CORRELATED SIGNALS & CAUSAL TRANSPORT OF SEA SURFACE TEMPERATURE ANOMALIES IN THE NORTH ATLANTIC

by
Stephen A. Jeffress

A dissertation submitted to Johns Hopkins University in conformity with the
requirements for the degree of Doctor of Philosophy

Baltimore, Maryland
October, 2014

Abstract

A sea surface temperature (SST) anomaly is a relatively warm or cold patch of water on the ocean surface. This thesis develops and applies a method for quantifying the transport of these anomalies in the midlatitude North Atlantic. Previous studies have estimated the advective transport from the time-lagged correlation of SST anomalies. We show that this approach does not consider diffusive SST transport or relaxation to atmospheric temperatures. The total transport is better quantified by the response function (Green's function) that solves the SST continuity equation for an impulsive external forcing. The impulse response framework clarifies the relationship between correlation and causation in the context of SST transport. The response function for North Atlantic satellite observed SST is estimated using a fluctuation-dissipation based inverse method. The method also provides a best fit linear operator that is decomposed into estimates of the SST velocity, diffusivity, and decay rate fields. The large scale features of the estimates compare favorably with previous studies. As far as we know, this thesis provides the first empirically derived estimate of an SST impulse response function. An unexplained result of our work is that mechanisms besides ocean currents appear responsible for the slow speed of SST anomaly propagation.

Acknowledgements

Many individuals have contributed to this thesis. Primary guidance was provided by Thomas W. N. Haine who is acknowledged for his generous support, patience, and diligence over several years. Funding sources include the Morton K. Blaustein Department of Earth and Planetary Sciences at Johns Hopkins University, and the National Science Foundation Grant #0801471 awarded to Lori Graham-Brady. Inspiring and productive conversations were held with Darryn W. Waugh, Anand Gnanadesikan, Gregory L. Eyink, Takeru Igusa, Mark Holzer, Inga M. Koszalka, Kial D. Stewart, Marcello G. Magaldi, Alex M. Fuller, Tristan Sharp, and Eshwan Ramudu.

Contents

List of Figures

Chapter 1

Introduction

A central question in oceanography and climate dynamics concerns the evolution of sea surface temperature (SST) anomalies. An SST anomaly is a relatively warm or cold patch of water on the ocean surface. In other words, it is a local fluctuation from the expected seasonal temperature that has a coherent spatial and temporal structure. These anomalies are important because they regulate the exchange of heat between the upper ocean and the atmosphere, profoundly influencing ocean circulation, weather, the seasonal cycle, low-frequency climate variability, and climate change.

The most successful approaches to analyzing the behavior of SST anomalies are based on the stochastic climate model approximation (Hasselmann, 1976). This approximation suggests that monthly to interannual fluctuations in SST are accurately represented as the integrated response of the upper ocean to a stochastic atmospheric forcing. The stochastic forcing is primarily composed of turbulent heat exchange between the ocean and atmosphere but also includes fluctuations in wind driven ocean currents and eddies (Frankignoul, 1985). The timescale of the forcing's decorrelation is assumed to be short, perhaps a few days, compared to the monthly timescale of SST anomalies. This separation of scales enables the application of statistical methods to identify physical mechanisms governing the transport of SST.

A common statistical method is to analyze the correlation of SST anomalies as a function of time-lag. Often the travel time, and hence advective speed, of a current flowing between two locations is estimated by the time-lag of greatest correlation between SST anomalies at each location. Sutton and Allen (1997) correlate ship-based SST timeseries and estimate an advective speed of 1.7 cm/s for low-frequency SST anomalies crossing the North Atlantic via the Gulf Stream. Chepurin and Carton (2012) apply this method to satellite SST data and suggest an advective speed of 2.7 cm/s in the North Atlantic Subpolar Gyre. Holliday et al. (2008) find surface current advection to be responsible for the 3-4 year peak timelag in SST anomalies crossing the Nordic Seas. The lagged correlation approach is also used to estimate the advection of salinity anomalies, most notably the Great Salinity Anomaly circulating at 3 cm/s in the Atlantic Subpolar Gyre in the 1970s (Dickson et al., 1988).

Chapter 2 of this thesis investigates the advantages and disadvantages of using the time-lagged correlation method to identify transport mechanisms. The major advantage is that the spatial and temporal lags allow physical processes with a range of timescales to be represented in the correlation. For example wintertime SST anomalies become isolated from the atmosphere in the summer seasonal thermocline and then re-emerge at a nearby location the following winter (Alexander et al., 1999). A multi-year lagged correlation analysis is capable of representing this process whereas a six-month lagged correlation is not. A disadvantage of this method is that it often requires a prohibitively-long timeseries to obtain convergent statistics. The length of the timeseries required is related to the decorrelation time of the forcing and the timescales present in the transport mechanisms (Jeffress and Haine, 2014b). Smoothing the data can shorten the required length, but this filters out the influence of the faster transport processes and leads to a low-frequency bias in estimates of the transport mechanisms.

There are also important reasons why the time lag of peak correlation would not provide a good estimate of underlying current speed. One reason is that SST anomalies may not be transported as a passive tracer. Non-linear dynamics and wave propagation may result in an effective velocity that does not reflect the speed or direction of the current. But even if SST is transported passively, the time-lag of peak correlation does not occur at the advective time in flows where the tracer is advected by currents, diffused by eddies, and decays into the atmosphere. This is shown in Chapter 2 by expressing the lagged correlation function in terms of the response function (Green's function) that solves the SST continuity equation for an impulsive forcing (Jeffress and Haine, 2014a). It is well established that the response function, if it can be obtained, is a highly insightful tool to diagnose tracer transport in the ocean and atmosphere (Haine and Hall, 2002; Hall and Plumb, 1994; Holzer and Hall, 2000;

Waugh and Hall, 2002). The reason is that the response function comprehensively quantifies the travel time distributions resulting from the combined influence of all transport mechanisms. In fact, the degree to which the lagged correlation function expresses a causal relationship is the degree to which the correlation function matches the response function. For this reason the framework in Chapter 2 clarifies the roles of correlation and causation in the context of stochastically forced and passively transported oceanic signals.

Another statistical approach to quantifying SST anomaly dynamics based on the stochastic climate approximation is the use of inverse modeling. The idea is to use SST observations to constrain the parameters of an underlying transport model. The parameters are the magnitudes of the individual transport mechanisms, such as advection, diffusion, and decay, at each grid point location. Piterbarg and Ostrovskii (1997) thoroughly describe this kind of procedure. If the SST anomalies are averaged over a large spatial region with slow currents and weak eddy activity, then advection and diffusion can be neglected and the spatially-dependent decay rate can be inverted by an autoregression. Frankignoul et al. (1998) use the autoregression approach to estimate anomaly persistence times (inverse of the decay rate) ranging from 30 to 120 days for SST anomalies averaged over a 5° × 5° grid in the midlatitude North Atlantic. A more advanced inverse method estimates the velocity, diffusivity, decay rate, and mixed layer entrainment rate of SST anomalies averaged over 2° to 3° grids in the North Pacific (Ostrovskii and Piterbarg, 2000) and North Atlantic (Ostrovskii and Font, 2003). The velocities estimated in these studies are not as fast as the underlying current speed, but they are faster than those estimated by the lagged correlation analysis. It may also be possible to use the inverse method in Ostrovskii and Font (2003) to estimate the SST response function described above. Calculating this function would be numerically challenging, however, because their inversion method is based on a discrete time-stepping model as opposed to a continuous-time evolution equation.

In Chapter 3 of this thesis we introduce an inverse method that is related to those outlined above, but is based on the more general framework of the fluctuation-dissipation theorem. The fluctuation-dissipation theorem suggests that under certain conditions the second order statistics of a system's fluctuations can be used to construct a linear operator that estimates the system's response to an external forcing (Nyquist, 1928; Callen and Welton, 1951). An active area of research is to apply this theorem to estimate the response of global circulation models to changes in model parameters (Gritsun and Branstator, 2007; Ring and Plumb, 2008). The same methodology applies to estimating the linear operator of a stochastically forced linear system such as SST fluctuations in the stochastic climate approximation (Penland and Sardeshmukh, 1995; Cooper and Haynes, 2011; Zanna, 2012). The major advantage of this approach is that the estimated response function is an analytic expression of the estimated linear operator. An additional advantage is that the linear operator can be decomposed into estimates of the time-average velocity field, diffusivity field, and decay rate field. The decomposition assumes that the linear operator comes from a spatial discretization of the continuous-space operator in an advection-diffusion-relaxation partial differential equation (PDE).

Chapter 4 applies an improved version of the method in chapter 3 to observed satellite SST data in the North Atlantic. The primary result is an estimated response function that comprehensively quantifies the transport of SST anomalies between any two locations in the North Atlantic. An additional result is the estimate of the velocity field, diffusivity field, and decay rate field that govern the North Atlantic transport of SST anomalies. Both the response function and estimates of the individual fields agree with previous studies, especially when the interesting effects of averaging scale are taken into consideration. We use SST anomaly data that is averaged over one day and 1/4° grid boxes. The aspect of our study that is least explained by previously known mechanisms is the slow speed of SST anomaly propagation compared to that of the underlying currents. As far as we know, this thesis provides the first empirically derived estimate of an SST impulse response function.

The Future work and Conclusion chapters provide a plan for future investigations and summarize the major findings of the thesis.

Chapter 2

Correlated signals and causal transport

This chapter is published by the Quarterly Journal of the Royal Meteorological Society (Jeffress and Haine, 2014a). It presents a framework for interpreting the time-lagged correlation of oceanographic data in terms of physical transport mechanisms. Previous studies have inferred aspects of ocean circulation by correlating fluctuations in temperature and salinity measurements at distant stations. Typically, the time-lag of greatest correlation is interpreted as an advective transit time and hence the advective speed of the current. In this chapter we relate correlation functions directly to the underlying equations of fluid transport. This is accomplished by expressing the correlation functions in terms of the Green's function of the transport equation. Two types of correlation functions are distinguished: field-forcing correlation and field-field correlation. Their unique relationships to the Green's function are illustrated in two idealized models of geophysical transport: a leaky pipe model and an advective-diffusive model. Both models show that the field-forcing correlation function converges to the Green's function as the characteristic (time or length) scale of forcing autocorrelation decreases. The leaky pipe model provides an explanation for why advective speeds inferred from time-lagged correlations are often less than the speed of the main current. The advective-diffusive model reveals a structural bias in the field-field correlation function when used to estimate transit times.

2.1 Introduction

One of the goals of oceanography is to characterize the pathways and speeds of the ocean's major currents. In pursuit of this goal, a common practice is to analyze correlations in oceanic measurements (such as temperature or salinity time series) from spatially-separated observation stations. Statistically significant correlations indicate a current flowing between the stations, and the time-lag at which the correlation is greatest measures the advective transit time and hence the current's mean advective speed.

Several studies employ this approach. Dickson et al. (1988) observe the time-lagged appearance of the *Great Salinity Anomaly* at several recording stations in the North Atlantic. The distance between stations and times of arrival suggest an average advection speed of 3 cm s^{-1} in the North Atlantic Subpolar Gyre. Similarly, Sutton and Allen (1997) correlate ship-based sea surface temperature (SST) anomalies crossing the North Atlantic. The time-lags of greatest correlation are used to suggest an average advection speed of 1.7 cm s^{-1}. A more recent example is Chepurin and Carton (2012) who suggest an advective speed of 2.7 cm s^{-1} in the North Atlantic from correlations of satellite-based SST data.

Although the practice is common, inferring advective speeds from lagged correlation invites criticism. A natural skepticism originates from the scientific principle that correlation does not imply causation (Yule, 1926). Why should the peak of the correlation be associated with the mean advective speed of the current? In fact there is some evidence to the contrary.

For example, Sutton and Allen (1997) note that their 1.7 cm s^{-1} estimate is considerably weaker than the 1 m s^{-1} current frequently observed in the Gulf Stream. The discrepancy is suggested to be due to weaker currents surrounding the Gulf Stream core.

A more in-depth look at a time-lagged correlation is found in Curry and McCartney (1996). Their study finds significant correlation in the oceanographic data recorded separately at Labrador Sea and Bermuda recording stations. Their primary message is that atmospheric conditions are first imprinted into the surface layer of the subpolar North Atlantic, and then transported to the subtropics by interior ocean currents. The plot of the correlation coefficient as a function of time-lag is Gaussian-like with a peak at six years and width of about 4 years. Curry and McCartney state that the transport from the Labrador Sea to Bermuda comprises multiple pathways and substantial mixing with other water masses. This suggests that the time-lagged correlation reflects not only the mean current speed, but the combined action of all advective-diffusive transport processes acting on the flow.

In this chapter we mathematically connect correlation functions to the underlying fluid transport equation. We do this by expressing correlation functions in terms of the Green's function solution to the transport equation. Green's functions have been used recently as a foundation for characterizing oceanic and atmospheric transport (e.g. Haine and Hall, 2002; Holzer and Hall, 2000; Hall and Plumb, 1994). The main advantage of this approach is that the Green's function contains complete information about the physical transport processes. By relating correlation functions and Green's functions, we provide a physically based framework for interpreting time-lagged correlations.

2.2 Mathematical Framework

The practice of time-lagged correlation analysis usually involves observable oceanic properties such as temperature, salinity, density, or tracer concentration. We refer to this observable quantity as the *field* variable $c(\mathbf{r}, t)$ at position $\mathbf{r}$ and time t, and assume it can be described by a linear partial differential equation of the form

$$\frac{d}{dt}c(\mathbf{r}, t) - \mathcal{L}(\mathbf{r}, t)c = q(\mathbf{r}, t). \tag{2.1}$$

Here $\mathcal{L}(\mathbf{r}, t)$ contains the linear transport operations such as advection and diffusion, and $q(\mathbf{r}, t)$ contains the sources and sinks of the field variable. If $c(\mathbf{r}, t)$ is a dynamically active property (e.g. temperature or salinity), it must first be verified that $c(\mathbf{r}, t)$ behaves as a passive tracer at the scales of interest (for SST anomalies see Piterbarg and Ostrovskii, 1997).

For simplicity of notation we use a spatially discrete version of (2.1),

$$\frac{d}{dt}\mathbf{c}(t) - \mathbf{A}(t)\mathbf{c}(t) = \mathbf{q}(t). \tag{2.2}$$

Here $\mathbf{c}(t)$ is an $N \times 1$ vector of field quantities at N spatial locations, $\mathbf{q}(t)$ contains the sources and sinks, and $\mathbf{A}(t)$ is an $N \times N$ spatial discretization of operator $\mathcal{L}$. The elements of $\mathbf{A}(t)$ are such that $A_{ij}(t)$ specifies the flux from location j to location i at time t. The spatial resolution of the discretization (2.2) can be increased to achieve the desired level of accuracy with the continuous form (2.1).

2.2.1 Time averaging

Equation (2.2) can be separated into its time average and fluctuating components by decomposing each of its variables,

$$\begin{aligned}
\mathbf{A}(t) &= \bar{\mathbf{A}} + \mathbf{A}'(t), \quad \bar{\mathbf{A}} = \tfrac{1}{2\ell}\textstyle\int_{-\ell}^{\ell}\mathbf{A}(t)dt \\
\mathbf{c}(t) &= \bar{\mathbf{c}} + \mathbf{c}'(t), \quad \bar{\mathbf{c}} = \tfrac{1}{2\ell}\textstyle\int_{-\ell}^{\ell}\mathbf{c}(t)dt \\
\mathbf{q}(t) &= \bar{\mathbf{q}} + \mathbf{q}'(t), \quad \bar{\mathbf{q}} = \tfrac{1}{2\ell}\textstyle\int_{-\ell}^{\ell}\mathbf{q}(t)dt.
\end{aligned} \tag{2.3}$$

The averages $\bar{\mathbf{A}}, \bar{\mathbf{c}}$ and $\bar{\mathbf{q}}$ exist if system (2.2) is in statistical equilibrium. This equilibrium is achieved if all eigenvalues of $\bar{\mathbf{A}}$ have negative real parts, or if the largest real eigenvalue of $\bar{\mathbf{A}}$ is zero and $\sum \bar{q}_i = 0$. The averages are captured accurately if time length ℓ is long compared to the slowest decaying eigenmode of $\bar{\mathbf{A}}$.

Inserting (2.3) into (2.2) and subtracting the time average leaves an equation for the evolution of fluctuations in the field variable,

$$\frac{d}{dt}\mathbf{c}'(t) = \bar{\mathbf{A}}\mathbf{c}'(t) + \mathbf{f}'(t), \tag{2.4}$$

where

$$\mathbf{f}'(t) = \mathbf{A}'(t)\mathbf{c}(t) - \overline{\mathbf{A}'(t)\mathbf{c}'(t)} + \mathbf{q}'(t). \tag{2.5}$$

Here we have created a *forcing* term $\mathbf{f}'(t)$ which combines the source term $\mathbf{q}'(t)$ and the terms involving the unsteady component of the circulation $\mathbf{A}'(t)$. Note that in (2.4) fluctuations of the field variable $\mathbf{c}'(t)$ originate from the forcing $\mathbf{f}'(t)$ and are transported by the (constant) mean circulation $\bar{\mathbf{A}}$.

2.2.2 Green's function solution

Following Boyce and DiPrima (1986), the solution to (2.4) is

$$\mathbf{c}'(t) = e^{\bar{\mathbf{A}}(t-t_0)}\mathbf{c}'(t_0) + \int_{t_0}^{t} e^{\bar{\mathbf{A}}(t-t')}\mathbf{f}'(t')dt', \tag{2.6}$$

where $\mathbf{c}'(t_0)$ is the initial condition at time t_0. The influence of this initial condition decays exponentially with the slowest decaying eigenmode of $\bar{\mathbf{A}}$. We assume this transient behavior can be neglected and write (2.6) as

$$\mathbf{c}'(t) = \int_{-\infty}^{\infty} \mathbf{G}(t-t')\mathbf{f}'(t')dt', \tag{2.7}$$

where

$$\mathbf{G}(\tau) = e^{\bar{\mathbf{A}}(\tau)} H(\tau). \tag{2.8}$$

Here the Green's function $\mathbf{G}(\tau)$ is an $N \times N$ matrix function of transit time $\tau = t - t'$. The Heaviside step function $H(\tau)$ restricts negative transit times which are unphysical.

It is important to note that the Green's function contains complete information about the pathways and transit times between any two locations in the flow. The individual element $G_{ij}(\tau)$ is a distribution of transit times (or response times) τ between an impulse in the forcing at location j and its arrival in the field at location i.

2.2.3 The field-forcing correlation function

There are several time correlation functions that can be constructed between two locations in system (2.4). The one most easily related to the Green's function is between the field and forcing variables. We call this the *field-forcing correlation* function and define it as

$$\mathbf{S_{cf}}(\tau) = \frac{1}{2\ell}\int_{-\ell}^{\ell} \mathbf{c}'(t)\mathbf{f}'^{\mathrm{T}}(t-\tau)dt \tag{2.9}$$

(sometimes called a cross-covariance). Here $\mathbf{S_{cf}}(\tau)$ has the same structure as the Green's function, i.e. an $N \times N$ matrix function of transit time τ. Note that the mean-removed signals, $\mathbf{c}'$ and $\mathbf{f}'$, are used instead of the original variables $\mathbf{c}$ and $\mathbf{f}$. The notation $\mathbf{S_{cf}}(\tau)$ instead of $\mathbf{S_{c'f'}}(\tau)$ is used for simplicity. The individual element $[S_{cf}(\tau)]_{ij}$ is the correlation between the field fluctuation at location i with the forcing fluctuation at location j. Positive τ means that the forcing events precede field events in time.

We define a similar correlation function between the forcing and itself, called the *forcing autocorrelation* function,

$$\mathbf{S_{ff}}(\tau) = \frac{1}{2\ell}\int_{-\ell}^{\ell} \mathbf{f}'(t)\mathbf{f}'^{\mathrm{T}}(t-\tau)dt. \tag{2.10}$$

Note $\mathbf{S_{ff}}(\tau)$ contains both the temporal and spatial correlation in the forcing. The individual element $[S_{ff}(\tau)]_{ij}$ is the correlation of the forcing at i with the forcing at j at time-lag τ. The spatial correlation of the forcing is contained in the off-diagonal elements of $\mathbf{S_{ff}}$. A white noise forcing (i.e. forcing which is zero mean, unit variance, and uncorrelated in time and space) has an autocorrelation function equal to the identity matrix multiplying a Dirac delta function, $\mathbf{S_{ff}}(\tau) = \mathbf{I}\delta(\tau)$.

To relate the field-forcing correlation function to the Green's function, multiply (2.7) by $\frac{1}{2\ell}\mathbf{f}'^{\mathrm{T}}(t-\tau)$ and integrate $\int_{-\ell}^{\ell} dt$. The result is

$$\mathbf{S}_{\mathbf{cf}}(\tau) = \int_{-\infty}^{\infty} \mathbf{G}(\tau - t')\mathbf{S}_{\mathbf{ff}}(t')dt'. \tag{2.11}$$

Here the field-forcing correlation function equals the Green's function smoothed by the forcing autocorrelation. The smoothing takes place in both space and time. The individual elements of (2.11) are

$$\left[S_{cf}(\tau)\right]_{ij} = \sum_k \int_{-\infty}^{\infty} G_{ik}(\tau - t') \left[S_{ff}(t')\right]_{kj} dt'. \tag{2.12}$$

Here $\left[S_{cf}(\tau)\right]_{ij}(\tau)$ is not simply $G_{ij}(\tau)$. If the forcing at j is correlated with the forcing at k, then $\left[S_{cf}(\tau)\right]_{ij}(\tau)$ is influenced by $G_{ik}(\tau)$. In contrast, if the forcing is white noise, (2.11) becomes

$$\mathbf{S}_{\mathbf{cf}}(\tau) = \int_{-\infty}^{\infty} \mathbf{G}(\tau - t')\mathbf{I}\delta(t')dt' = \mathbf{G}(\tau). \tag{2.13}$$

In this case the field-forcing correlation function equals the Green's function. More generally, if the times and distances of the forcing's autocorrelation are small compared to the intrinsic scales of the transport, then the overlap of $\mathbf{G}(\tau - t')$ and $\mathbf{S}_{\mathbf{ff}}(t')$ in (2.11) is small. In this case (2.13) is a good approximation, and the field-forcing correlation function provides an *unbiased* estimate of the Green's function. This is demonstrated by two examples in section 2.3.

2.2.4 The field-field correlation function

Another relevant correlation function is between field fluctuations at two locations, $c'_i(t)$ and $c'_j(t)$. We define this *field-field correlation* $\mathbf{S_{cc}}(\tau)$ as

$$\mathbf{S_{cc}}(\tau) = \frac{1}{2\ell}\int_{-\ell}^{\ell} \mathbf{c}'(t)\mathbf{c}'^{\mathrm{T}}(t-\tau)dt. \tag{2.14}$$

Multiplying (2.7) by $\frac{1}{2\ell}\mathbf{c}'^{\mathrm{T}}(t-\tau)$, integrating $\int_{-\ell}^{\ell} dt$, and inserting (2.11) yields

$$\mathbf{S_{cc}}(\tau) = \int_{-\infty}^{\infty} \mathbf{S_{cf}}(\tau + t'')\mathbf{G}^{\mathrm{T}}(t'')dt''. \tag{2.15}$$

This formula relates the field-field correlation function to the Green's function and (implicitly) $\mathbf{S_{ff}}$ (from 2.11). It is evident that $\mathbf{S_{cc}}(\tau)$ is a less precise estimator of the Green's function than the field-forcing correlation function. The reason is that $\mathbf{S_{cf}}(\tau)$ is already a smoothed version of the Green's function (2.11), and (2.15) involves an additional space-time smoothing.

Also, as opposed to field-forcing correlation, field-field correlation is a *biased* estimator of the Green's function. Equation (2.13) shows that with white noise forcing, the field-forcing correlation function equals the Green's function. This is not the case for field-field correlation. Equation (2.15) can be written

$$\mathbf{S_{cc}}(\tau) = \iint_{-\infty}^{\infty} \mathbf{G}(t')\mathbf{S_{ff}}(\tau - t' + t'')\mathbf{G}^{\mathrm{T}}(t'')dt'dt''. \tag{2.16}$$

For white noise forcing,

$$\mathbf{S_{cc}}(\tau) = \int_{-\infty}^{\infty} \mathbf{G}(\tau + t')\mathbf{G}^{\mathrm{T}}(t')dt'. \tag{2.17}$$

The correlation between field fluctuations at two locations, $c_i'(t)$ and $c_j'(t)$, is

$$[S_{cc}(\tau)]_{ij} = \sum_k \int_{-\infty}^{\infty} G_{ik}(\tau + t')G_{jk}(t')dt'. \tag{2.18}$$

Thus even with uncorrelated forcing, the field-field correlation function is composed of Green's function contributions from multiple sources. Specifically, $[S_{cc}(\tau)]_{ij}$ is the superposition of the convolutions of the Green's function from all source points k to field point i with the Green's function from all source points k to field point j. The field-field correlation function does not converge to the Green's function as the forcing autocorrelation decreases. This makes the field-field correlation function a biased estimator of the Green's function.

Although it is biased in general, we are aware of two special cases in which the field-field correlation function provides an unbiased estimate of the Green's function. These are:

1. When the forcing is uncorrelated in time and has a specific pattern of spatial correlation. Specifically, $\mathbf{S_{ff}}$ has a spatial structure proportional to $\bar{\mathbf{A}} + \bar{\mathbf{A}}^{\mathrm{T}}$.
2. When the forcing is uncorrelated in both time and space, and $\bar{\mathbf{A}}$ is symmetric. In this case the time derivative of the field-field correlation function is proportional

to the Green's function (see Snieder, 2006, for example).

We provide the details of these cases in appendices 2.A and 2.B. Both cases are attractive areas for future research, but the specific pattern of forcing spatial correlation (case 1) seems unlikely to occur naturally, and advection is not a symmetric transport operator (case 2). Thus these cases are not obviously relevant for ocean circulation.

2.3 Illustrative examples

We illustrate the relationship between correlation functions and Green's functions with two tangible examples. Both models are widely applied in practice, and demonstrate the theory in a spatially continuous form.

2.3.1 Leaky Pipe Model

The first example is the *leaky pipe* model. We choose this model for the following reasons:

1. Leaky pipe models are commonly used to describe the transport of tracers in geophysical flows (e.g. Waugh and Hall, 2005; Neu and Plumb, 1999; Pickart et al., 1989).
2. The model is spatially continuous with an analytical Green's function solution.
3. The leaking action leads to multiple pathways between any two locations in the

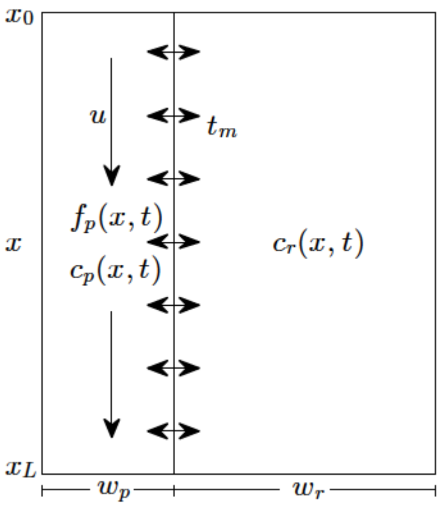

Figure 2.1: The leaky pipe model consists of two coupled regions: a pipe region of width w_p and uniform flow u, and a reservoir region of width w_r and no interior flow. A flux of passive tracer $f_p(x,t)$ is injected into the pipe randomly. Mixing between the pipe and reservoir occurs at rate $1/t_m$. The concentration of tracer in the pipe and reservoir is $c_p(x,t)$ and $c_r(x,t)$, respectively. There is no inflow of tracer at x_0. Tracer flows freely out of the model at x_L.

pipe.

4. The model provides an explanation for why advective speeds inferred from time-lagged correlation are often slower than the speed of the main current.

An illustration of the model is given in Fig. 2.1. A random flux of passive tracer $f_p(x,t)$ is injected into the pipe. The spatial and temporal correlation of the tracer injection is defined by,

$$S_{ff}(x,x',\tau) = \frac{1}{2\ell}\int_{-\ell}^{\ell} f_p'(x,t)f_p'(x',t-\tau)dt. \tag{2.19}$$

Here $f'_p(x,t)$ denotes the mean-subtracted fluctuation in $f_p(x,t)$ according to (2.3). The fluctuations are Gaussian correlated in time, and uncorrelated in space.

$$S_{ff}(x,x',\tau) = \frac{1}{\sigma_\tau\sqrt{2\pi}}\exp\left(-\frac{\tau^2}{2\sigma_\tau^2}\right)\delta(x-x'), \tag{2.20}$$

Here σ_τ is the time-lag at which the forcing's autocorrelation has been reduced by 1/e.

The concentrations of tracer in the pipe and reservoir are $c_p(x,t)$ and $c_r(x,t)$. The concentrations evolve in response to the tracer forcing by

$$\begin{aligned} \frac{\partial c_p}{\partial t} + u\frac{\partial c_p}{\partial x} + \frac{1}{t_m}(c_p - c_r) &= f_p(x,t) \\ \frac{\partial c_r}{\partial t} - \frac{\alpha}{t_m}(c_p - c_r) &= 0 \end{aligned} \tag{2.21}$$

(Waugh and Hall, 2005). Here $\alpha = w_p/w_r$ is the ratio of the pipe and reservoir widths. Neglecting the transient behavior associated with the initial condition, the solution of the pipe concentration is

$$c_p(x,t) = \int_{-\infty}^{\infty}\int_{x_0}^{x_L} G(x,x',t-t')f_p(x',t')dx'dt' \tag{2.22}$$

(for the solution of c_r see Terenzi and Hall, 2010). The Green's function $G(x,x',\tau)$ relates the tracer injected at (x',t') to its arrival at (x,t). The time $\tau = t - t'$ is the time between injection and arrival. This time is not *only* due to the pipe current speed u. Instead, the mixing with the reservoir results in a distribution of times from

x' to x. This distribution is given by the Green's function, viz.,

$$\begin{aligned} G(x,x',\tau) = {} & \frac{1}{ut_m}\sqrt{\frac{\alpha(x-x')}{uT}}\exp\left(\frac{x'-x-\alpha uT}{ut_m}\right) \\ & \times I_1\left\{\frac{2}{t_m}\sqrt{\frac{\alpha(x-x')T}{u}}\right\}H(T) \\ & + \frac{1}{u}\exp\left(\frac{x'-x}{ut_m}\right)\delta(T). \end{aligned} \tag{2.23}$$

Here $T = \tau - \frac{1}{u}(x-x')$, and I_1 is the modified Bessel function of order 1 (Terenzi and Hall, 2010).

The Green's function (Fig. 2.2) gives the distribution of transit times between two locations in the leaky pipe model. The model parameters ($u = 5$ cm s^{-1}, $t_m = 0.1$ yr^{-1}, $\alpha = 0.1$) are chosen to be relevant to oceanic transport. The time for the current u to travel between x_1 and x_2 is 1 year (vertical dashed grey line). In contrast, the timescale for the tracer transport is between 5 and 20 years. The difference is due to mixing with the reservoir.

Field-forcing correlation in the leaky pipe model

In this section we show how the field-forcing correlation function S_{cf} relates to the Green's function in the leaky pipe model. The time-lagged correlation of the time series of tracer concentration at x_2 with the time series of tracer injection at x_1 is,

$$S_{cf}(x_2,x_1,\tau) = \frac{1}{2\ell}\int_{-\ell}^{\ell} c'_p(x_2,t)f'_p(x_1,t-\tau)dt. \tag{2.24}$$

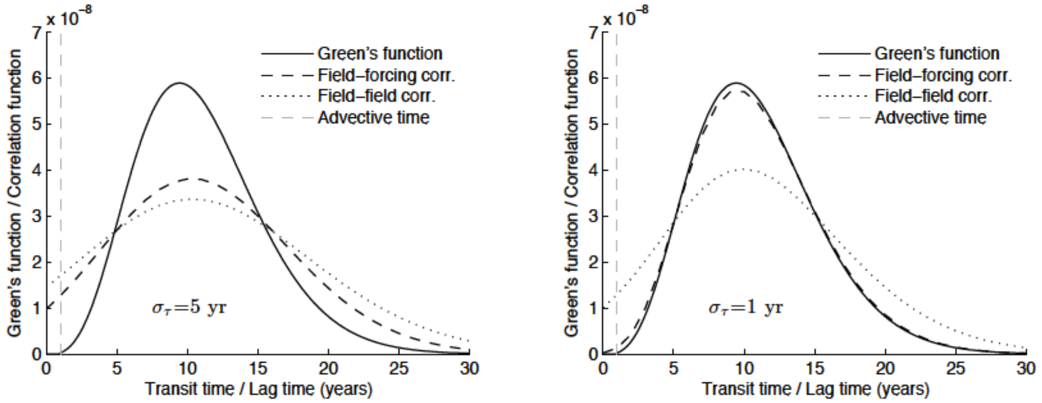

Figure 2.2: Leaky pipe model comparison of the Green's function and correlation functions for a large (left panel) and small (right panel) timescale of forcing autocorrelation. The Green's function gives the distribution of transit times between two locations in the model. The field-forcing correlation function (dashed line) converges to the Green's function as σ_τ, the timescale of the forcing autocorrelation, decreases. The normalized field-field correlation function (dotted line) does not converge to the Green's function. The vertical dashed grey line indicates the advective timescale. The parameters for the leaky pipe model are $u = 5$ cm s^{-1}, t_m=0.1 yr^{-1}, and $\alpha = w_p/w_r = 0.1$. The units of the Green's function, field-forcing correlation function, and field-field correlation function are m^{-1}, $[c]^2$, and $[c]^2$ s, respectively.

Here τ is the time-lag and c'_p, f'_p are the mean-removed fluctuations in c_p and f_p following (2.3). Proceeding as in section 2.2.3, the relationship between the field-forcing correlation function and the Green's function is

$$S_{cf}(x_2, x_1, \tau) = \iint G(x_2, x', \tau - t')S_{ff}(x', x_1, t')dx'dt'. \qquad (2.25)$$

Inserting the autocorrelation of the tracer forcing (2.20) into (2.25) yields

$$S_{cf}(x_2, x_1, \tau) = \int_{-\infty}^{\infty} \frac{G(x_2, x_1, \tau - t')}{\sigma_\tau\sqrt{2\pi}} \exp\left(\frac{-t'^2}{2\sigma_\tau^2}\right) dt'. \qquad (2.26)$$

Thus the correlation of the tracer concentration at x_2 and tracer forcing at x_1 is the Green's function from x_1 to x_2 smoothed in time by the autocorrelation of the tracer forcing at x_1.

Fig. 2.2 shows the result. For a tracer injection with large temporal autocorrelation (left panel, $\sigma_\tau = 5$ years), the forcing-field correlation function (dashed line) is a smoothed version of the Green's function. The presence of smoothing is indicated by the positive correlation at $\tau = 0$, which implies infinite speeds of travel, if naively interpreted as $G(x_2, x_1, 0)$. As the autocorrelation vanishes (right panel, $\sigma_\tau = 1$ year) field-forcing correlation converges to the Green's function. This shows that if the timescale of the transport is long compared to the timescale of the forcing autocorrelation, the field-forcing correlation function provides an unbiased estimate of the Green's function.

Field-field correlation in the leaky pipe model

The field-field correlation function S_{cc} does not relate to the Green's function the same way as S_{cf}. The correlation of observed tracer concentrations at x_1 and x_2 is

$$S_{cc}(x_2, x_1, \tau) = \frac{1}{2\ell} \int_{-\ell}^{\ell} c_p'(x_2, t) c_p'(x_1, t - \tau) dt \tag{2.27}$$

Proceeding as described in section 2.2.4, the relationship between the field-field correlation function and the Green's function is

$$\begin{aligned} S_{cc}(x_2, x_1, \tau) = & \iiiint dx' dt' dx'' dt'' \\ & G(x_2, x', t') S_{ff}(x', x'', \tau - t' + t'') G(x_1, x'', t''). \end{aligned} \tag{2.28}$$

Here two Green's functions are superposed and smoothed by the forcing autocorrelation. Inserting the expression for the autocorrelation (2.20) yields,

$$S_{cc}(x_2,x_1,\tau) = \iiint dx'dt'dt'' \frac{G(x_2,x',t')G(x_1,x',t'')}{\sigma_\tau\sqrt{2\pi}} \exp\left\{\frac{(\tau - t' + t'')^2}{-2\sigma_\tau^2}\right\}. \tag{2.29}$$

Thus the correlation between the field at x_1 and the field at x_2 is influenced by Green's functions from multiple source locations x'. Even with vanishing temporal correlation in the forcing ($\sigma_\tau \to 0$), we find

$$S_{cc}(x_2,x_1,\tau) = \iint G(x_2,x',\tau + t')G(x_1,x',t')dx'dt', \tag{2.30}$$

which retains the influence from all source locations x'.

A comparison of the Green's function with the normalized field-field correlation function is shown in Fig 2.2. The field-field correlation function (dotted line) is a less accurate estimator of the Green's function than the field-forcing correlation function. The reason is that $S_{cc}(x_2,x_1,\tau)$ is a smoothed version of $S_{cf}(x_2,x_1,\tau)$ (2.15). The field-field correlation function also does not approach the Green's function as the forcing autocorrelation decreases from $\sigma_\tau = 5$ years to $\sigma_\tau = 1$ year. Instead it converges to a complex superposition of Green's function convolutions from multiple source locations (2.28).

Fig 2.2 also suggests an explanation for the discrepancy between current speeds in-

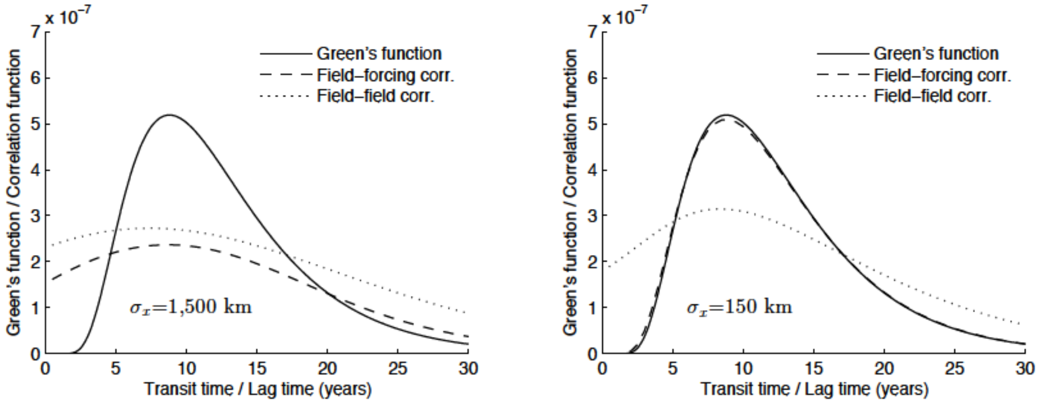

Figure 2.3: Advective-diffusive model comparison of the Green's function and correlation functions for a large (left panel) and small (right panel) spatial scale of forcing autocorrelation. The Green's function gives the distribution of transit times between two locations ($x_1 - x_2 = 1,575$ km). The field-forcing correlation function converges to the Green's function as σ_x, the spatial scale of the forcing autocorrelation, decreases. The normalized field-field correlation function does not converge to the Green's function in the same way. Instead it converges to a shape noticeably biased towards shorter transit times. The model parameters are $u = .5$ cm s^{-1}, $k = 10^3$ m^2 s^{-1}. The units of the Green's function, field-forcing correlation function, and field-field correlation function are m^{-1}, $[c]^2$, and $[c]^2$ s, respectively.

ferred from correlation and those directly measured. The time-lag of greatest correlation, for both correlation functions, is roughly 10 years. In contrast, the timescale of the advective current u is only 1 year (vertical dashed line). If the time-lag of greatest correlation were used to estimate the current speed, the result would be 0.5 cm s^{-1} instead of the true speed of 5 cm s^{-1}. The explanation is that the time-lag of greatest correlation estimates the modal time of the Green's function, not the advective time.

2.3.2 Advective-diffusive model

The one-dimensional advective-diffusive model is another common idealization of geophysical flows. It illustrates additional aspects of the relationship between the Green's function and correlation functions. Specifically, it shows the impact of spatial correlation in the forcing, and the structural bias in the field-field correlation function.

In this model temperature anomalies are advected and diffused throughout a one-dimensional infinite pipe. The pipe is randomly heated at all locations x and times t. The pipe's temperature $c(x,t)$ responds to this heating according to the advection-diffusion equation,

$$\frac{\partial c}{\partial t} + u\frac{\partial c}{\partial x} - k\frac{\partial^2 c}{\partial x^2} = f(x,t). \tag{2.31}$$

Here u is a constant, uniform advection speed and k is a constant, uniform diffusivity. The random heating $f(x,t)$ is uncorrelated in time and Gaussian correlated in space,

$$S_{ff}(x,x',\tau) = \frac{1}{\sigma_x\sqrt{2\pi}}\exp\left\{-\frac{(x-x')^2}{2\sigma_x^2}\right\}\delta(\tau). \tag{2.32}$$

The solution to (2.31) can be written in a form similar to (2.22). In this case the Green's function is

$$G(x,x',\tau) = \frac{1}{2\sqrt{\pi k\tau}}\exp\left\{-\frac{(x-x'-u\tau)^2}{4k\tau}\right\}. \tag{2.33}$$

The time-integrated Green's function Z, mean transit time Γ, and width Δ are

$$\mathrm{Z} = 1/u, \qquad \Gamma = \frac{2k}{u^2} + \frac{(x-x')}{u}, \qquad \Delta = 2\sqrt{\frac{k\,(x-x')}{u^3}}, \tag{2.34}$$

for $u, k, x-x' > 0$. Derivations of these quantities are provided in Appendix 2.C.

Differences from a familiar model

A more familiar model of advective-diffusive transport is the semi-infinite pipe with a boundary source. (e.g. Haine and Hall, 2002; Rehder et al., 1999; Rhein, 1994). This model is well suited for tracers injected into the ocean surface (a boundary) and subsequently mixed into the interior. The transit time distribution (TTD) from the boundary to the interior is a type of Green's function known as a *boundary propagator*. The boundary propagator for the semi-infinite pipe is an attractive form for fitting observed data because it is an Inverse Gaussian distribution with well defined properties.

Despite these advantages, the semi-infinite boundary source model is not ideal for our purposes. The main reason is that the forcing only occurs in one location, i.e. the boundary, which is an over-simplification in the present context. Other reasons are as follows:

1. Allowing interior forcing, not just boundary forcing, is more appropriate for spatially continuous variables with spatially continuous forcing (e.g. SST anomalies).

2. The forcing defined in (2.5) includes the non-steady component of the transport. Thus the possibility of interior forcing due to unsteady flow should be maintained even when the boundary is the only source.

3. The important role of the forcing's spatial autocorrelation cannot be illustrated with a single forcing location.

4. The boundary propagator is defined differently than the Green's function of section 2.2. The boundary propagator is the response to an impulse in the boundary condition, instead of a response to an impulsive source within the system. To relate these two types of Green's functions see Holzer and Hall (2000).

Correlations in the advective-diffusive model

The field-forcing correlation function in the advective-diffusive model is

$$S_{cf}(x_2, x_1, \tau) = \int\limits_{-\infty}^{\infty} \frac{G(x_2, x', \tau)}{\sigma_x \sqrt{2\pi}} \exp\left\{ \frac{(x_1 - x')^2}{2\sigma_x^2} \right\} dx'. \tag{2.35}$$

Here the Green's function is smoothed spatially instead of temporally (2.26). The field-field correlation function is

$$\begin{aligned} S_{cc}(x_2, x_1, \tau) = \iiint dt' dx' dx'' \\ \frac{G(x_2, x', \tau + t') G(x_1, x'', t')}{\sigma_x \sqrt{2\pi}} \exp\left\{ \frac{(x' - x'')^2}{-2\sigma_x^2} \right\}. \end{aligned} \tag{2.36}$$

The integral over time acts to blend the Green's function of x_2, x' with the Green's function of x_1, x''. This biases $S_{cc}(x_2, x_1, \tau)$ as an estimator of $G(x_2, x_1, \tau)$.

Fig. 2.3 compares correlation functions and the Green's function in the advective-diffusive model. The field-forcing correlation function converges to the Green's function as the spatial scale of the forcing autocorrelation decreases from $\sigma_x = 1,500 km$

(left panel) to $\sigma_x = 150km$ (right panel). In contrast, the field-field correlation function does not give the Green's function as σ_x vanishes. Instead the upstream transport of the advective diffusive model, $G(x, x', \tau) > 0$ for $x < x'$, contributes additional non-zero convolutions to the field-field correlation function (2.29). The result is a function that is noticeably biased to shorter transit times compared to the Green's function.

2.4 Chapter summary

Part of the difficulty in explaining correlations in oceanic data is the lack of a theoretical framework which connects correlation functions to the underlying equations of fluid transport. In this chapter we provide that framework. The key theoretical insight is that correlation functions can be related to the Green's function of the transport equations, and the Green's function contains complete information about the physical transport processes.

The framework can be used to explain the discrepancy between current speeds inferred from correlation and those directly measured. The reason is that the time-lag of greatest correlation should be related to the modal time of the Green's function, not the current's advective time, or mean transport time. The leaky pipe model illustrates this difference explicitly.

We distinguish between two types of correlation functions, each with a different relationship to the Green's function. The forcing-field correlation function converges to the Green's function as the scales of forcing autocorrelation decrease. This was illustrated for temporally correlated forcing in the leaky pipe model, and for spatially correlated forcing in the advective-diffusive model. In contrast, the field-field correlation function does converge to the Green's function as the forcing autocorrelation vanishes. As shown by the advective-diffusive model, the structural bias in the field-field correlation function arises from a complex superposition of overlapping Green's functions. This bias should be investigated further, perhaps with insight from the special cases provided in Appendix B.

This work also suggests the possibility of using correlation functions to fit the distribution parameters of an idealized transport model. For example the time-lagged correlation of air/sea heat flux anomalies (forcing) and SST anomalies (field) could be fitted to an advective-diffusive transport model using the field-forcing correlation relationship (2.11) and the distribution parameters given in (2.34).

Finally, the relationships between correlation functions and Green's functions (2.11) and (2.16) extend beyond geophysical fluid transport. They hold for a broad class of linear systems (2.2) which are used extensively in the physical sciences, social sciences, and engineering. The use of correlation functions to analyze large datasets, and the accompanying need to distinguish correlation from causation, is similarly pervasive. Less common is the use of Green's functions to quantify causal mechanisms in linear systems. We are unaware of a previous formulation linking correlation functions and Green's functions using the discretized operator $\mathbf{A}$. We advocate this approach to interpret correlation functions.

2.5 Chapter appendix

2.A Forcing with specific pattern of spatial correlation

A special relationship between the field-field correlation function and the Green's function arise due to a specific form of spatial pattern of forcing autocorrelation. This relationship can be seen by introducing the adjoint Green's function and making the following argument in the frequency domain.

In the time domain, the forward Green's function $\mathbf{G}(\tau)$ satisfies

$$\left(\frac{d}{d\tau}\mathbf{I} - \bar{\mathbf{A}}\right)\mathbf{G}(\tau) = \mathbf{I}\delta(\tau), \tag{2.37}$$

and the adjoint Green's function $\mathbf{G}^{\dagger}(\tau)$ satisfies

$$\left(-\frac{d}{d\tau}\mathbf{I} - \bar{\mathbf{A}}^{\mathrm{T}}\right)\mathbf{G}^{\dagger}(\tau) = \mathbf{I}\delta(\tau). \tag{2.38}$$

The reciprocity relationship between the forward and adjoint Green's function is

$$\mathbf{G}^{\mathrm{T}}(\tau) = \left\{\mathrm{e}^{\bar{\mathbf{A}}\tau}H(\tau)\right\}^{\mathrm{T}} = \mathrm{e}^{\bar{\mathbf{A}}^{\mathrm{T}}\tau}H(\tau) = \mathbf{G}^{\dagger}(-\tau). \tag{2.39}$$

Using the Fourier transform convention

$$\tilde{\mathbf{f}}(\omega) = \mathcal{F}\left\{\mathbf{f}(t)\right\} = \int_{-\infty}^{\infty}\mathbf{f}(t)\mathrm{e}^{-i\omega t}dt \tag{2.40}$$

$$\mathbf{f}(t) = \mathcal{F}^{-1}\left\{\tilde{\mathrm{f}}(\omega)\right\} = \frac{1}{2\pi}\int_{-\infty}^{\infty}\tilde{\mathrm{f}}(\omega)\mathrm{e}^{-i\omega t}d\omega, \tag{2.41}$$

the frequency domain representations of the forward and adjoint Green's function are

$$\left(i\omega\mathbf{I} - \bar{\mathbf{A}}\right)\tilde{\mathbf{G}}(\omega) = \mathbf{I} \tag{2.42}$$

$$\left(-i\omega\mathbf{I} - \bar{\mathbf{A}}^{\mathrm{T}}\right)\tilde{\mathbf{G}}^{\dagger}(\omega) = \mathbf{I}. \tag{2.43}$$

Reciprocity in the frequency domain is

$$\tilde{\mathbf{G}}^{\mathrm{T}}(\omega) = \tilde{\mathbf{G}}^{\dagger *}(\omega), \tag{2.44}$$

where the asterisk denotes a complex conjugate. Equation (2.16) in the frequency domain is

$$\tilde{\mathbf{S}}_{\mathbf{cc}}(\omega) = \tilde{\mathbf{G}}(\omega)\tilde{\mathbf{S}}_{\mathbf{ff}}(\omega)\tilde{\mathbf{G}}^{\dagger}(\omega), \tag{2.45}$$

where the convolution theorem,

$$\mathcal{F}\left\{\int_{-\infty}^{\infty} f(t-t')g(t')dt'\right\} = \tilde{f}(\omega)\tilde{g}(\omega) \tag{2.46}$$

has been applied. Multiplying (2.43) by the forward Green's function yields

$$\tilde{\mathbf{G}}\left(-i\omega\mathbf{I} - \bar{\mathbf{A}}^{\mathrm{T}}\right)\tilde{\mathbf{G}}^{\dagger} = \tilde{\mathbf{G}}, \tag{2.47}$$

(suppressing the dependence on frequency ω for convenience). Using the reciprocity relationship (2.44), the transposed complex conjugate of (2.47) is

$$\tilde{\mathbf{G}}\left(i\omega\mathbf{I}-\bar{\mathbf{A}}\right)\tilde{\mathbf{G}}^{\dagger}=\tilde{\mathbf{G}}^{\dagger}. \tag{2.48}$$

Adding (2.47) to (2.48) gives

$$\tilde{\mathbf{G}}+\tilde{\mathbf{G}}^{\dagger}=-\tilde{\mathbf{G}}\left(\bar{\mathbf{A}}+\bar{\mathbf{A}}^{\mathrm{T}}\right)\tilde{\mathbf{G}}^{\dagger}. \tag{2.49}$$

If the autocorrelation of the forcing can be decomposed into a spatially uniform temporal component $q(t)$, and a constant spatial component that is proportional to $\bar{\mathbf{A}}+\bar{\mathbf{A}}^{\mathrm{T}}$, then its Fourier transform is

$$\tilde{\mathbf{S}}_{\mathbf{ff}}(\omega)=-a\tilde{q}(\omega)\left(\bar{\mathbf{A}}+\bar{\mathbf{A}}^{\mathrm{T}}\right). \tag{2.50}$$

Inserting (2.50) into (2.49) yields

$$\tilde{\mathbf{G}}+\tilde{\mathbf{G}}^{\dagger}=\frac{1}{a\tilde{q}}\tilde{\mathbf{G}}\tilde{\mathbf{S}}_{\mathbf{ff}}\tilde{\mathbf{G}}^{\dagger}. \tag{2.51}$$

Inserting (2.45) into (2.51) yields

$$\tilde{\mathbf{G}}+\tilde{\mathbf{G}}^{\dagger}=\frac{1}{a\tilde{q}}\tilde{\mathbf{S}}_{\mathbf{cc}}. \tag{2.52}$$

In the time domain (2.52) is

$$\mathbf{S_{cc}}(\tau) = a \int_{-\infty}^{\infty} \left\{ \mathbf{G}(\tau - t') + \mathbf{G}^{\dagger}(\tau - t') \right\} q(t') dt'. \tag{2.53}$$

Here the field-field correlation function is the superposition of the forward and adjoint Green's functions smoothed by the temporal correlation of the forcing. If the forcing is uncorrelated in time, $q(t) = \delta(t)$, then

$$\mathbf{S_{cc}}(\tau) = a\mathbf{G}(\tau) + a\mathbf{G}^{\dagger}(\tau). \tag{2.54}$$

Due to causality, $\mathbf{G}^{\dagger}(\tau) = 0$ for $\tau > 0$, thus (2.54) becomes

$$\mathbf{S_{cc}}(\tau > 0) = a\mathbf{G}(\tau). \tag{2.55}$$

2.B Symmetric transport operator

Another special relationship between the field-field correlation function and the Green's function occurs when the transport matrix $\bar{\mathbf{A}}$ is symmetric and the forcing is uncorrelated. In this case subtracting (2.47) from (2.48) yields

$$\tilde{\mathbf{G}} - \tilde{\mathbf{G}}^{\dagger} = -2i\omega\tilde{\mathbf{G}}\tilde{\mathbf{G}}^{\dagger}. \tag{2.56}$$

Inserting the Fourier transform of (2.17) into (2.56) yields

$$\tilde{\mathbf{G}} - \tilde{\mathbf{G}}^{\dagger} = -2i\omega\tilde{\mathbf{S}}_{\mathbf{cc}}. \tag{2.57}$$

For positive τ the time domain representation of (2.57) is

$$2\frac{d}{d\tau}\mathbf{S}_{\mathbf{cc}}(\tau > 0) = -\mathbf{G}(\tau). \tag{2.58}$$

In this case the time derivative of the field-field correlation function is proportional to the Green's function.

2.C Parameters of the Green's function of the one-dimensional infinite advective-diffusive pipe

Here we derive parameters of the distribution of transit times between two points in an advective diffusive flow along a 1-dimensional infinite pipe (2.31). Each parameter below is defined for $u > 0, k > 0$ and $x - x' > 0$. The time-integrated Green's function Z is

$$\begin{aligned} \mathrm{Z} &= \int_{-\infty}^{\infty} G(x, x', \tau) d\tau \\ &= \int_{-\infty}^{\infty} \frac{1}{2\sqrt{\pi k \tau}} \exp\left\{ -\frac{(x - x' - u\tau)^2}{4k\tau} \right\} d\tau \\ &= \frac{1}{u}. \end{aligned} \tag{2.59}$$

The mean transit time Γ is

$$\begin{aligned}\Gamma &= \frac{1}{\mathrm{Z}}\int_{-\infty}^{\infty}\tau G(x,x',\tau)d\tau \\ &= u\int_{-\infty}^{\infty}\frac{\tau}{2\sqrt{\pi k\tau}}\exp\left\{-\frac{(x-x'-u\tau)^2}{4k\tau}\right\}d\tau \\ &= \frac{2k}{u^2}+\frac{(x-x')}{u}. \end{aligned} \tag{2.60}$$

The width Δ is

$$\begin{aligned}2\Delta^2 &= \frac{1}{\mathrm{Z}}\int_{-\infty}^{\infty}(\tau-\Gamma)^2 G(x,x',\tau)d\tau \\ &= u\int_{-\infty}^{\infty}\frac{(\tau-\Gamma)^2}{2\sqrt{\pi k\tau}}\exp\left\{-\frac{(x-x'-u\tau)^2}{4k\tau}\right\}d\tau \\ &= \frac{4k(x-x')}{u^3}. \end{aligned} \tag{2.61}$$

Note that Δ^2 is half the variance of the distribution.

Chapter 3

Estimating SST transport from SST fluctuations

This chapter is published in the New Journal of Physics (Jeffress and Haine, 2014b). It introduces a method to quantify the transport of sea surface temperature (SST) from SST fluctuations. Previous studies have estimated the advective transport of SST from time-lag correlation of SST anomalies. However this approach does not consider diffusive SST transport or relaxation to atmospheric temperatures. To quantify the transport more completely we use a response function (Green's function) which solves the SST continuity equation for an impulsive forcing. The response function is estimated from SST anomalies using a fluctuation-dissipation approach. An assumption of spatial locality in the linear operator used to produce the response significantly improves the accuracy of the method. Using 100 years of data from a stochastically-forced prototypical SST model, the method estimates the SST transport response function to within 10% error. Decomposing the linear operator into symmetric, anti-symmetric, and divergent operators enables estimates of the model's spatially dependent velocity vector, diffusivity tensor, and relaxation rate which converge at the same rate as the response function.

3.1 Introduction

Accurate estimates of sea-surface temperature (SST) transport are fundamental to predicting climate change. One method to obtain such estimates is to analyze the propagation of anomalously warm and cold patches of water (SST anomalies) in surface currents. Advective transport times are often identified by the time-lag of greatest correlation between time series of SST anomalies at remote locations Sutton and Allen (1997); Hansen and Bezdek (1996); Chepurin and Carton (2012). The disadvantage of this approach is that the modal time of the two-point correlation function does not necessarily occur at the advective time in flows where SST anomalies are advected by currents, diffused by eddies, and relaxed to atmospheric temperatures.

A more complete quantification of the transport is given by the response function (Green's function) which solves the SST continuity equation for an impulsive forcing. Instead of a single advective time, the Green's function gives the distribution of travel times that arise from the complex interactions of advection, diffusion and relaxation. This approach has provided a foundation for quantifying the transport of a variety of tracers in geophysical reservoirs Haine and Hall (2002); Hall and Plumb (1994);

Waugh and Hall (2002). If SST arises from a stochastic atmospheric forcing Hasselmann (1976) and is advected and diffused over certain temporal and spatial scales Piterbarg and Ostrovskii (1997), then the transport response function is related to correlation functions by the covariance structure of the atmospheric forcing Jeffress and Haine (2014a).

An alternative method of estimating transport from SST anomalies may be possible using the fluctuation-dissipation theorem. Under certain conditions, natural fluctuations of a system can be used to construct a linear operator that estimates the system's response to an external forcing Nyquist (1928); Callen and Welton (1951). It has been suggested that the climate has properties which approximately satisfy the required conditions Leith (1975); Majda et al. (2005) and the theorem has recently been used to estimate response functions in global circulation models Gritsun and Branstator (2007); Ring and Plumb (2008). If the system can be modeled by a set of stochastically-forced linear differential equations, then estimating the linear operator amounts to an inverse modeling problem Cooper and Haynes (2011); Achatz et al. (2013). The linear stochastic model has shown to be a good approximation of SST anomaly dynamics in the tropical Pacific Penland and Sardeshmukh (1995), North Atlantic Zanna (2012), and on a global scale Newman (2007).

This article combines and builds upon the body of work outlined above. We use a fluctuation-dissipation approach including the inverse linear method to estimate the time-average SST transport response from SST anomalies. We make a spatial locality assumption in the calculation of the linear operator that significantly improves the accuracy of the response function and enables estimates of individual field parameters in the transport equation. In section 3.2 the method is described for a generic physical system. In section 3.3 we apply the method to a prototypical numerical model of SST transport. A summary of the results and future work is provided in section 3.4.

3.2 Mathematical framework

3.2.1 Time average of a continuous model

The method we present applies to physical systems that can be usefully modeled by stochastically-forced linear partial differential equations,

$$\frac{d}{dt}c(\mathbf{x},t) - \mathcal{L}(\mathbf{x},t)c = q(\mathbf{x},t). \tag{3.1}$$

Here the field variable c and the stochastic source term q vary over space $\mathbf{x}$ and time t. The linear operator $\mathcal{L}$ contains spatial derivatives and coefficients that also depend on space and time.

Let each term in (3.1) be the sum of a time-mean (denoted by $^-$) and fluctuation (denoted by $'$) component,

$$\begin{aligned} c(\mathbf{x},t) &= \bar{c}(\mathbf{x}) + c'(\mathbf{x},t) \\ \mathcal{L}(\mathbf{x},t) &= \bar{\mathcal{L}}(\mathbf{x}) + \mathcal{L}'(\mathbf{x},t) \\ q(\mathbf{x},t) &= \bar{q}(\mathbf{x}) + q'(\mathbf{x},t). \end{aligned} \tag{3.2}$$

We are interested in statistically-steady solutions to (3.1) so we assume that $\bar{c}$, $\bar{\mathcal{L}}$ and $\bar{q}$ are well defined and disregard transient behavior associated with the initial condition. Inserting (3.2) into (3.1) and subtracting the time-mean leaves an equation for fluctuations in the field variable,

$$\frac{d}{dt}c' - \bar{\mathcal{L}}c' = f'(\mathbf{x}, t), \tag{3.3}$$

where

$$f'(\mathbf{x}, t) = \mathcal{L}'\bar{c} + \mathcal{L}'c' - \overline{\mathcal{L}'c'} + q'. \tag{3.4}$$

Here we have created a time-varying forcing term f' which sums fluctuations in the source term with fluctuations in the operator acting on the field. Note that this forcing has zero time mean because $\overline{q'} = \overline{\mathcal{L}'\bar{c}} = 0$ and $\overline{\mathcal{L}'c'} - \overline{\overline{\mathcal{L}'c'}} = 0$.

3.2.2 Spatial discretization

A spatial discretization of (3.3) is

$$\frac{d}{dt}\mathbf{c}'(t) - \mathbf{B}\mathbf{c}' = \mathbf{f}'(t). \tag{3.5}$$

Here $\mathbf{c}'(t)$ and $\mathbf{f}'(t)$ are $M \times 1$ vectors of field and forcing fluctuations, respectively, at M spatial locations. The $M \times M$ matrix $\mathbf{B}$ is a discretization of the time-average continuous operator $\bar{\mathcal{L}}$. The system is stable if all eigenvalues of $\mathbf{B}$ have negative real parts. It has been shown that (3.5) provides an accurate model of SST anomaly dynamics for characterization and predictive purposes Penland and Sardeshmukh (1995); Zanna (2012).

The $M \times M$ response (Green's) function $\mathbf{G}(t)$ is given by (3.5) with an impulsive forcing at each location,

$$\frac{d}{dt}\mathbf{G}(t) - \mathbf{B}\mathbf{G} = \mathbf{I}\delta(t), \tag{3.6}$$

where $\mathbf{I}\delta(t)$ is an $M \times M$ identity matrix multiplying a Dirac delta function. The solution of (3.6) is $\mathbf{G}(t) = \mathrm{e}^{\mathbf{B}t}$, and the solution of (3.5) is

$$\mathbf{c}'(t) = \int_{-\infty}^{t} \mathbf{G}(t-s)\mathbf{f}'(s)ds, \tag{3.7}$$

where we have assumed causality $\mathbf{G}(t<0)=0$.

Note that the frequency content of $\mathbf{c}'$ in (3.7) results from the smoothing of $\mathbf{f}'$ by $\mathbf{G}$. If the forcing's temporal autocorrelation is negligible (white in time), which has been found to be a good approximation for the forcing of linearized SST dynamics at monthly timescales Penland and Sardeshmukh (1995); Zanna (2012), then the timescales of variability in $\mathbf{c}'(t)$ results from the distribution of timescales in $\mathbf{G}$. In this case the timescales in $\mathbf{G}$ determine the length of a sample of $\mathbf{c}'$ that is required to accurately estimate the system's equilibrium statistics.

3.2.3 Response estimation - global method

Now consider that we possess a sufficiently long timeseries of $\mathbf{c}'(t)$ and wish to produce estimates (denoted by ˆ) of the discrete operator $\mathbf{B}$ and response function $\mathbf{G}(\mathrm{t})$. Using the fluctuation-dissipation approach by way of the inverse modeling method Cooper and Haynes (2011), we multiply (3.5) by $\mathbf{c}'^{\mathrm{T}}$ and then average over time,

$$\overline{\frac{d}{dt}\mathbf{c}'\mathbf{c}'^{\mathrm{T}}} - \mathbf{B}\overline{\mathbf{c}'\mathbf{c}'^{\mathrm{T}}} = \overline{\mathbf{f}'\mathbf{c}'^{\mathrm{T}}}. \tag{3.8}$$

As discussed above we assume the temporal autocorrelation of the forcing is negligible. This implies that the covariance between $\mathbf{c}'$ and $\mathbf{f}'$ at zero time lag is also negligible, and a least squares minimization of $\overline{\mathbf{f}'\mathbf{c}'^{\mathrm{T}}}$ provides an estimate for the discrete operator,

$$\hat{\mathbf{B}} = \overline{\frac{d}{dt}\mathbf{c}'\mathbf{c}'^{\mathrm{T}}}\left(\overline{\mathbf{c}'\mathbf{c}'^{\mathrm{T}}}\right)^{-1}. \tag{3.9}$$

The corresponding estimated response function is

$$\hat{\mathbf{G}}(t) = \mathrm{e}^{\hat{\mathbf{B}}t}. \tag{3.10}$$

We refer to (3.9) as the *global method* because $\overline{\mathbf{c}'\mathbf{c}'^{\mathrm{T}}}$ contains all $M \times M$ covariances in the system. In practice the covariance matrices of high dimensional systems often have high condition numbers and cannot be inverted accurately, so measures are taken to reduce the dimensionality of the system. Empirical orthogonal function (EOF) decomposition is a common strategy for dimensionality reduction (e.g.Zanna

(2012)), but our interest is in quantifying the transport in physical space instead of EOF space, so we take a different approach.

3.2.4 Response estimation - local method

The *local method* assumes spatial locality in the linear operator in order to reduce the dimension of the inverted covariance matrix in (3.9). This approach assumes that the dominant physical processes in $\bar{\mathcal{L}}$ can be expressed as local spatial derivatives, such as advection and diffusion. In addition we assume that the spatial scale of these process acting over the timestep of interest is smaller than the size of the stencil used in the localization. We are interested in monthly SST propagation, so the size of the stencil must be larger than the characteristic advective-diffusive propagation distance of an SST anomaly in one month.

If the discretization of $\bar{\mathcal{L}}c'$ at each grid point m is confined to a local spatial stencil of N neighbors surrounding m, then $\mathbf{B}$ is a sparse matrix with sparse rows $\mathbf{b}_m$ for $m = 1, 2, 3, ..., M$,

$$\mathbf{B} = [\mathbf{b}_1; \mathbf{b}_2; \mathbf{b}_3; ... ; \mathbf{b}_M]\,. \tag{3.11}$$

Let the $1 \times N$ row vector $\widetilde{\mathbf{b}}_m$ be the *stencil-only* subset of nonzero elements in $\mathbf{b}_m$. Following steps (3.5)-(3.9), the estimate of $\mathbf{B}$ is

$$\hat{\widetilde{\mathbf{b}}}_m = \overline{\frac{d}{dt} c'_m \widetilde{\mathbf{c}'}^{\mathrm{T}}_m} \left(\overline{\widetilde{\mathbf{c}}'_m \widetilde{\mathbf{c}'}^{\mathrm{T}}_m} \right)^{-1}, \tag{3.12}$$

where $\widetilde{\mathbf{c}}'_m$ is the corresponding $N \times 1$ stencil-only subset of $\mathbf{c}'$, and c'_m is element m of $\mathbf{c}'$.

The local method changes the single $M \times M$ matrix inversion in (3.9) to several $N \times N$ matrix inversions in (3.12). This essentially removes the noisy, non-neighboring covariances from the calculation. Assuming the conditions of locality mentioned above are appropriate, this will improve the estimates of $\mathbf{B}$ and $\mathbf{G}(t)$ for a sample of $\mathbf{c}'(t)$ of a given length, compared to the global method.

3.2.5 Decomposing a centered stencil

For a centered stencil such as the one to the right, we can separate $\hat{\mathbf{B}}$ into components that act symmetrically, anti-symmetrically, and divergently about the central point. In contrast to the common symmetric-antisymmetric matrix decomposition, this method pairs matrix elements on the same row $\hat{B}_{mn}$ and $\hat{B}_{mn'}$, where for each stencil neighbor n of center cell m, the opposing neighbor is n'.

	n	
	m	
	n'	

Stencil

Letting $\hat{\mathbf{B}} = \hat{\mathbf{S}} + \hat{\mathbf{A}}$, the operator that acts symmetrically $\hat{\mathbf{S}}$ is

$$\hat{S}_{mn} \;= \tfrac{1}{2}\left(\hat{B}_{mn} + \hat{B}_{mn'}\right), \tag{3.13}$$

and the operator that acts anti-symmetrically $\hat{\mathbf{A}}$ is

$$\hat{A}_{mn} \;= \tfrac{1}{2}\left(\hat{B}_{mn} - \hat{B}_{mn'}\right), \tag{3.14}$$

for all neighbors n of all grid cells m. If sums along the rows of $\hat{\mathbf{B}}$ are not zero, then $\hat{\mathbf{B}}$ contains a divergent part $\hat{\mathbf{J}}$ which is diagonal,

$$\hat{J}_{mm} = \textstyle\sum_n \hat{B}_{mn}. \tag{3.15}$$

This decomposition is useful when $\hat{\mathbf{S}}$, $\hat{\mathbf{A}}$, and $\hat{\mathbf{J}}$, can be used to distinguish local physical processes in $\bar{\mathcal{L}}$. In the next section we use $\hat{\mathbf{S}}$ to estimate the SST diffusion, $\hat{\mathbf{A}}$ to estimate SST advection, and $\hat{\mathbf{J}}$ to estimate the rate at which SST relaxes to atmospheric conditions.

3.3 SST transport model

3.3.1 Model description

We now apply the method described above to a model of SST transport. The model is a stochastically-forced two-dimensional heat transport equation in a Cartesian plane. The continuous equation satisfies (3.3) where $c'(\mathbf{x}, t)$ is the SST fluctuation in space

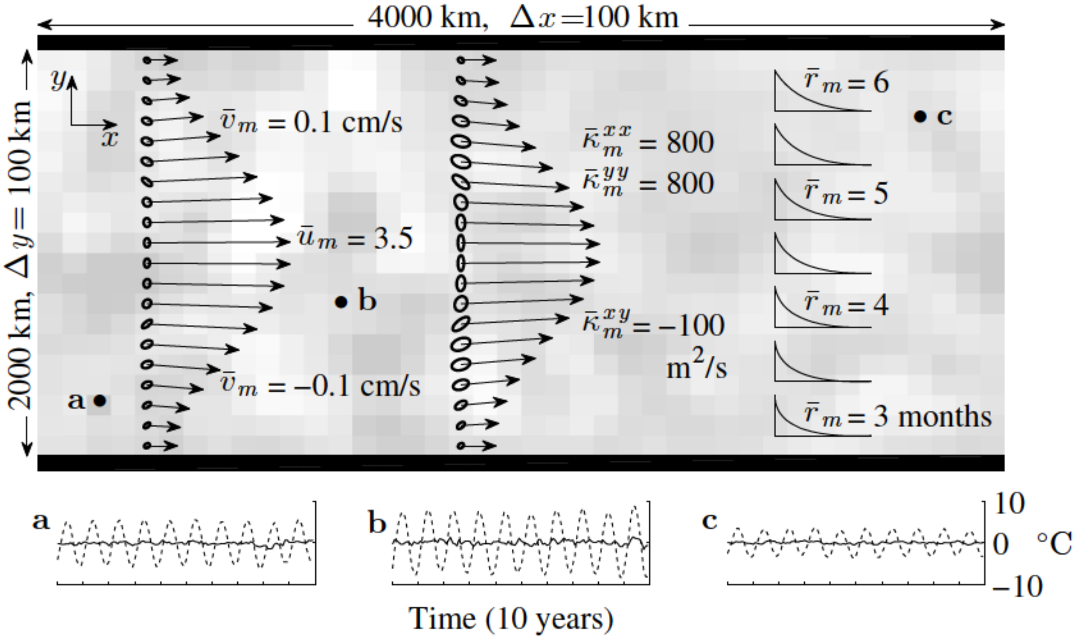

Figure 3.1: Schematic of the SST model. The flow is periodic in zonal direction x and has no flux through the boundaries of meridional direction y. The advective current (arrows) is strongest in the zonal direction and in the center of the channel. Weaker currents near the boundaries and in the meridional direction maintain a non-divergent velocity field. Diffusivities (ellipses) are smallest near the boundaries and greatest just above and below the strong central current. The timescale for SST relaxation decreases in the meridional direction (exponential curves). A snapshot of the monthly SST anomaly field (background grayscale image) indicates the characteristic width of an SST anomaly (300 km). Time series of the SST (dashed line) and anomaly (solid line) at locations **a**, **b** and **c** show the varying magnitude of the seasonal cycle and anomaly at these locations.

$\mathbf{x} = [x, y]$ and time t. The model's SST transport operator is

$$\bar{\mathcal{L}} = \nabla \cdot \bar{\mathbf{K}}(\mathbf{x})\nabla - \bar{\mathbf{u}}(\mathbf{x}) \cdot \nabla - \bar{r}(\mathbf{x}) \tag{3.16}$$

which is the time-average of a velocity vector $\mathbf{u} = [u(\mathbf{x}, t); v(\mathbf{x}, t)]$, symmetric diffusivity tensor $\mathbf{K} = [\kappa^{xx}(\mathbf{x}, t), \kappa^{xy}(\mathbf{x}, t); \kappa^{xy}(\mathbf{x}, t), \kappa^{yy}(\mathbf{x}, t)]$, and relaxation rate $r(\mathbf{x}, t)$. The diffusivity is a continuous parameterization of all molecular and turbulent mixing processes occurring below a finite spatial scale Δ, the velocity represents the average advective current over Δ, and the relaxation rate is the timescale for an SST anomaly of size Δ to relax to the atmospheric temperature. The structure of the flow is illustrated in figure 3.1. The values of the flow parameters are chosen to represent observed SST transport Sutton and Allen (1997).

The continuous equations are spatially discretized to satisfy (3.5). The rectangular grid (figure 3.1) has a total of $M = W \times H$ cells with W horizontal cells of size Δx and H vertical cells of size Δy. The discretization of $\bar{\mathcal{L}}c'$ uses a central differencing stencil,

$$
\begin{aligned}
\bar{\kappa}^{xx}{}_m \frac{\partial^2}{\partial x^2} c'_m &\approx \frac{\bar{\kappa}^{xx}_m}{\Delta x^2} \left(c'_{m+1} - 2c'_m + c'_{m-1} \right) \\
\bar{\kappa}^{yy}{}_m \frac{\partial^2}{\partial y^2} c'_m &\approx \frac{\bar{\kappa}^{yy}_m}{\Delta y^2} \left(c'_{m+W} - 2c'_m + c'_{m-W} \right) \\
2\bar{\kappa}^{xy}{}_m \frac{\partial^2}{\partial x \partial y} c'_m &\approx \frac{2\bar{\kappa}^{xy}_m}{\Delta x \Delta y} \left(c'_{m+W+1} - 2c'_m + c'_{m-W-1} \right) \\
\frac{\partial \bar{\kappa}^{xx}_m}{\partial x} \frac{\partial}{\partial x} c'_m &\approx \frac{\bar{\kappa}^{xx}_{m+1} - \bar{\kappa}^{xx}_{m-1}}{4\Delta x^2} \left(c'_{m+1} - c'_{m-1} \right) \\
\frac{\partial \bar{\kappa}^{yy}_m}{\partial y} \frac{\partial}{\partial y} c'_m &\approx \frac{\bar{\kappa}^{yy}_{m+W} - \bar{\kappa}^{yy}_{m-W}}{4\Delta y^2} \left(c'_{m+W} - c'_{m-W} \right) \\
\frac{\partial \bar{\kappa}^{xy}_m}{\partial x} \frac{\partial}{\partial y} c'_m &\approx \frac{\bar{\kappa}^{xy}_{m+1} - \bar{\kappa}^{xy}_{m-1}}{4\Delta x \Delta y} \left(c'_{m+W} - c'_{m-W} \right) \\
\frac{\partial \bar{\kappa}^{xy}_m}{\partial y} \frac{\partial}{\partial x} c'_m &\approx \frac{\bar{\kappa}^{xy}_{m+W} - \bar{\kappa}^{xy}_{m-W}}{4\Delta x \Delta y} \left(c'_{m+1} - c'_{m-1} \right) \\
\bar{u}^x_m \frac{\partial}{\partial x} c'_m &\approx \frac{\bar{u}^x_m}{2\Delta x} \left(c'_{m+1} - c'_{m-1} \right) \\
\bar{u}^y_m \frac{\partial}{\partial y} c'_m &\approx \frac{\bar{u}^y_m}{2\Delta y} \left(c'_{m+W} - c'_{m-W} \right).
\end{aligned}
\tag{3.17}
$$

Cell number m increases from the bottom-left to the top-right in figure 3.1 such that $m-1, m+1, m-W$ and $m+W$ are the left, right, bottom and top neighbors, respectively. The terms in (3.17) together with the relaxation rate $\bar{r}_m$ and boundary conditions comprise the discretized transport operator $\mathbf{B}$ in (3.5).

The model's forcing is generated randomly with a defined covariance structure and SST fluctuations are produced by integrating (3.7) numerically with a time step Δt = 1 month. The forcing has zero temporal decorrelation time (white in time) and its spatial decorrelation distance is tuned to produce SST anomalies characteristic of those seen in the Gulf Stream region of the Hadley Centre Sea Ice and Sea Surface Temperature dataset Rayner et al. (2003). The time series below the schematic in

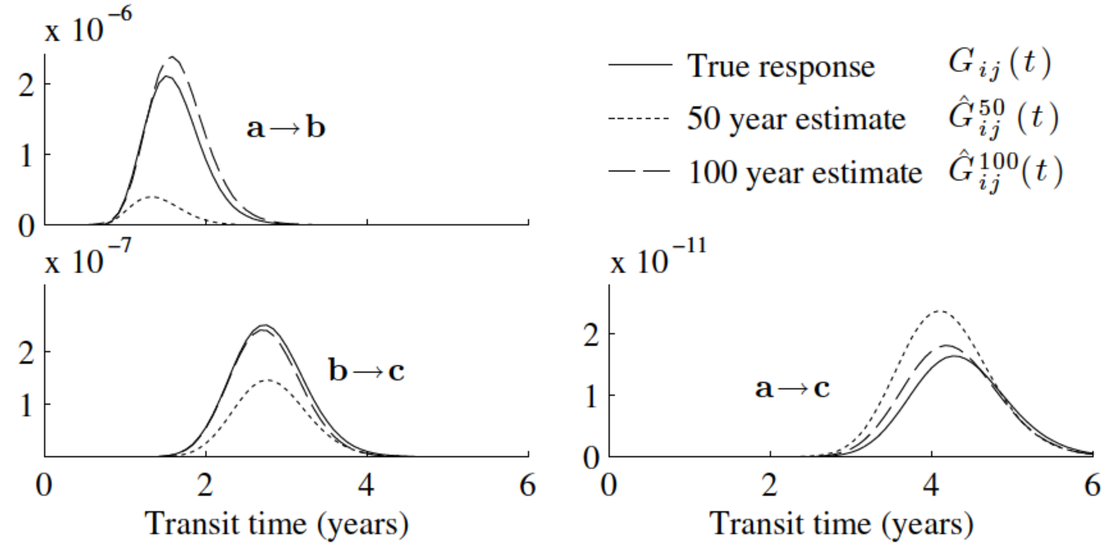

Figure 3.2: True and estimated response functions for SST transport between locations **a**, **b** and **c** in figure 3.1. The response arrives sooner (later) and has larger (smaller) magnitude between locations that are spatially close (far) such as **a**→**b** (**a**→**c**). With 50 years of model output, the estimated response function captures the order of magnitude and timescale of transit accurately. After 100 years the estimated response is within 10% of the true response.

figure 3.1 shows 10 years of SST fluctuations for model locations $\mathbf{a}, \mathbf{b}$ and $\mathbf{c}$. The anomaly signal is obtained by removing the average 12-month seasonal cycle from the SST fluctuation time series.

The transport between locations $\mathbf{a}, \mathbf{b}$ and $\mathbf{c}$ is quantified by elements $G_{ab}(t)$, $G_{bc}(t)$, and $G_{ac}(t)$ of the true response function $\mathbf{G}(t)$ as shown (by the solid lines) in figure 3.2. The **a**→**b** response arrives sooner and has a larger magnitude than the **a**→**c** response because **a** is nearer to **b** than **c**. However it is not the case (as might naively be assumed) that the time-lag of peak response results only from the advection, the width results from the diffusion, and the magnitude results from the relaxation. Instead these properties of the response function arise from a complex interaction of the individual mechanisms.

3.3.2 Estimating the transport response and flow parameters

We now estimate the model's SST transport response function and flow parameters using the SST anomaly time series. We estimate the discretized operator $\hat{\mathbf{B}}$ using the local method (3.12) where $\mathbf{c}'(t)$ is a finite length time series of monthly SST anomalies. The estimated response $\hat{\mathbf{G}}(t)$ is calculated by inserting $\hat{\mathbf{B}}$ into (3.10). Figure 3.2 shows elements of the estimated response $\hat{G}_{ab}(t)$, $\hat{G}_{bc}(t)$ and $\hat{G}_{ac}(t)$ using 50 and 100 years of SST data. The order of magnitude and timescale of transport are accurately captured by the 50 year estimate. With 100 years, the average error in the logarithm of $\hat{\mathbf{G}}(t)$ is approximately 10%.

Parameters of the flow are estimated by separating $\hat{\mathbf{B}}$ into symmetric, antisymmetric, and divergent operators (3.13)-(3.15). Estimates of the velocity vector, diffusivity

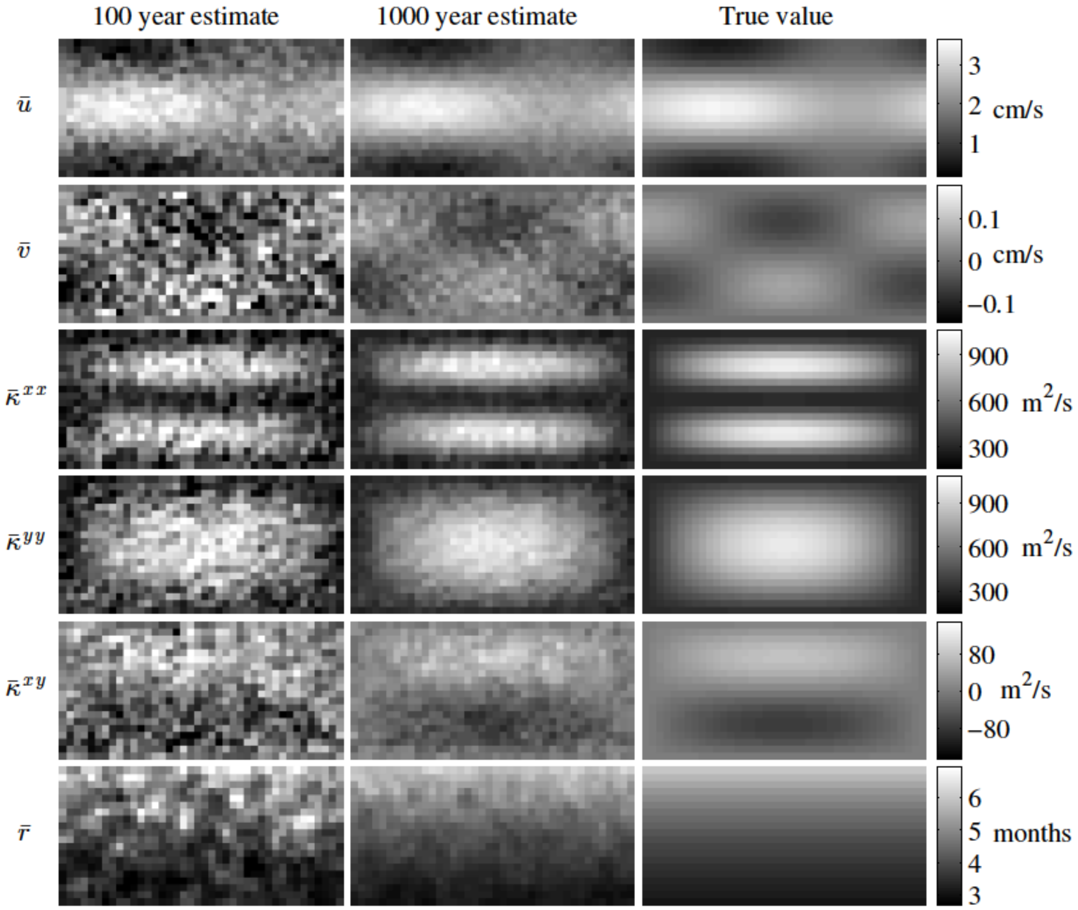

Figure 3.3: True and estimated velocity vector $(\bar{u}, \bar{v})$, diffusivity tensor $(\bar{\kappa}^{xx}, \bar{\kappa}^{yy}, \bar{\kappa}^{xy})$, and relaxation rate $(\bar{r})$. The true value of each flow parameter (right column) has a unique spatial pattern. This pattern is visible in the estimates made with 100 years of SST data (left columnn). After 1000 years (center column) the average error in the flow parameter estimates is 3-5%.

tensor, and relaxation are obtained by

$$\begin{aligned}
\hat{\hat{\kappa}}_m^{xx} &= \Delta x^2 \hat{S}_{m,m+1} \\
\hat{\hat{\kappa}}_m^{yy} &= \Delta y^2 \hat{S}_{m,m+W} \\
2\hat{\hat{\kappa}}_m^{xy} &= \Delta x \Delta y \hat{S}_{m,m+W+1} \\
\frac{\widehat{\partial \bar{\kappa}}_m^{xx}}{\partial x} &= \tfrac{1}{2\Delta x}\left(\hat{\hat{\kappa}}_{m+1}^{xx} - \hat{\hat{\kappa}}_{m-1}^{xx}\right) \\
\frac{\widehat{\partial \bar{\kappa}}_m^{yy}}{\partial y} &= \tfrac{1}{2\Delta y}\left(\hat{\hat{\kappa}}_{m+W}^{yy} - \hat{\hat{\kappa}}_{m-W}^{yy}\right) \\
\frac{\widehat{\partial \bar{\kappa}}_m^{xy}}{\partial x} &= \tfrac{1}{2\Delta x}\left(\hat{\hat{\kappa}}_{m+1}^{xy} - \hat{\hat{\kappa}}_{m-1}^{xy}\right) \\
\frac{\widehat{\partial \bar{\kappa}}_m^{xy}}{\partial y} &= \tfrac{1}{2\Delta y}\left(\hat{\hat{\kappa}}_{m+W}^{xy} - \hat{\hat{\kappa}}_{m-W}^{xy}\right) \\
\hat{\hat{u}}_m^{x} &= -2\Delta x \hat{A}_{m,m+1} + \tfrac{1}{2\Delta x}\tfrac{\widehat{\partial \bar{\kappa}}_m^{xx}}{\partial x} + \tfrac{1}{2\Delta y}\tfrac{\widehat{\partial \bar{\kappa}}_m^{xy}}{\partial y} \\
\hat{\hat{u}}_m^{y} &= -2\Delta y \hat{A}_{m,m+W} + \tfrac{1}{2\Delta y}\tfrac{\widehat{\partial \bar{\kappa}}_m^{yy}}{\partial y} + \tfrac{1}{2\Delta x}\tfrac{\widehat{\partial \bar{\kappa}}_m^{xy}}{\partial x} \\
\hat{\hat{r}}_m &= \hat{J}_{mm}.
\end{aligned} \tag{3.18}$$

Figure 3.3 shows estimates of the flow parameters using 100 and 1,000 years of SST model output. The true value of each flow parameter (right column) has a unique spatial pattern which is visible in the estimates made with 100 years of data (left column). With 1000 years (center column), the errors in the estimates is 3-5%.

Figure 3.4 shows the convergence of $\hat{\mathbf{G}}, \hat{\hat{u}}, \hat{\hat{\kappa}}^{xx}$ and $\hat{\hat{r}}$ as the length ℓ of the SST time series increases from 10 to 10,000 years. The error decreases as $1/\sqrt{\ell}$ for each quantity. For a given ℓ, estimates of the velocity and relaxation rate are more accurate than the diffusivity and less accurate than the response. The difference in accuracy of the flow parameters appears to be related to their relative magnitudes in the transport

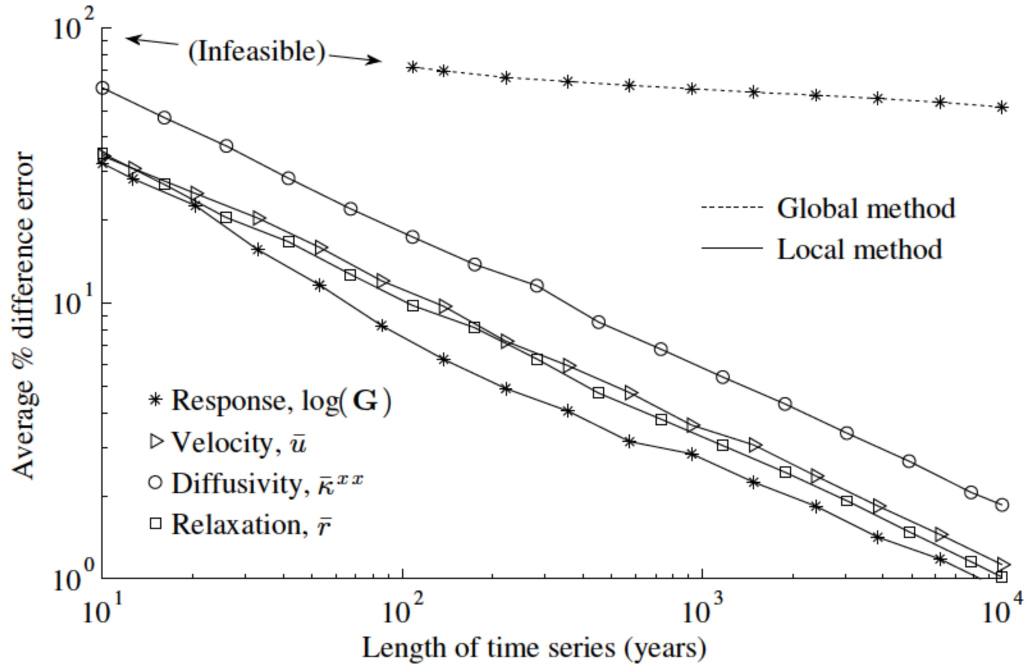

Figure 3.4: Convergence of the estimates of the transport response function and flow parameters with increasing SST data. The average % difference error with increasing time series length ℓ is shown for $\hat{\bar{u}}, \hat{\bar{\kappa}}^{xx}, \hat{\bar{r}}$ and the base 10 logarithm of $\hat{\mathbf{G}}$. Using the local method (3.12) the error decreases as $1/\sqrt{\ell}$. The locality assumption also makes it possible to estimate the velocity vector, diffusivity tensor, and relaxation rates which converge at the same rate. The global method (3.9) cannot reliably estimate a response with $\ell < 100$ years because of the condition number of the covariance matrix is too large. For $100 < \ell < 10,000$ years, the error in the global method's response function decreases only marginally due to noisy covariances between non-neighboring grid locations.

operator (the magnitude of the average velocity in the antisymmetric operator is 4 times greater than the average diffusivity in the symmetric operator). We expect the response to be more accurate than the flow parameters because the calculation of the response (3.10) averages random errors in the parameter fields. A more thorough analysis of these differences is an area for future investigation.

Figure 3.4 also shows the error in the response function estimated by the global method (3.9) which does not assume locality in the linear operator. This method cannot reliably produce a response estimate with less than 100 years because the condition number of $\overline{\mathbf{c}'\mathbf{c}'^{\mathrm{T}}}$ is too large. Between 100 and 10,000 years the error in the global method's response decreases only marginally. The reason is that even when $\overline{\mathbf{c}'\mathbf{c}'^{\mathrm{T}}}$ can be inverted, it is dominated by the noisy covariances of non-neighboring locations. Inverting the covariance matrices in the local method (3.12) is more accurate because non-neighboring covariances have been removed. A local assumption is also required to estimate the velocity, diffusivity, and relaxation rates, so they do not appear for the global method in figure 3.4.

3.4 Chapter summary

The goal of this study is to demonstrate a method for estimating SST transport information from a field of SST anomaly time series. Using 100 years of output from a stochastically-forced SST model (figure 3.1) the method estimates the SST transport response function to within 10% error (figure 3.2). A key aspect of our approach is assuming spatial locality in the linear operator (3.12) used to construct the response. This significantly reduces noise that otherwise prohibits the required inversion of the anomaly covariance matrix. The locality assumption also enables estimates of the model's spatially dependent velocity vector, diffusivity tensor, and relaxation rates (figure 3.3) which converge at the same rate as the response function (figure 3.4).

We intend to use this method to estimate response functions in global circulation models and climatological datasets. We hope the method will provide independent estimates of SST transport in the North Atlantic to compare with previous studies. The transport of other oceanographic properties such as salinity or ocean color can be estimated using the same approach. More generally, the method presented here may be used to estimate atmospheric or other climatic response functions when the spatial locality assumption applies.

Chapter 4

The transport of North Atlantic SST anomalies

This chapter investigates the dynamics of satellite observed SST anomalies in the midlatitude North Atlantic. We use a fluctuation-dissipation based inversion method that estimates the linearized dynamics of SST fluctuations. The estimated linear operator is used to construct the response function (Green's function) that solves the SST continuity equation for an impulsive heat source driving SST. The estimated response function is rich in information because it estimates both the timescales and magnitude of the SST anomaly transport between every pair of locations in the field. The assumption that the linear operator comes from a spatially discretized advection-diffusion-relaxation partial differential equation enables estimates of the velocity field, diffusivity field, and decay rate field. The $\sim$5 cm/s advection field, $\sim$1000 m^2/s eddy diffusivity field, and $\sim$20 day decay timescale compare favorably with previous studies.

These results confirm that the best-fit velocity field for SST anomaly propagation is unambiguously different from the surface current velocity. A plan to investigate the mechanisms responsible for this difference is provided as future work (Chapter 5).

4.1 Introduction

This chapter investigates the dynamics of these anomalies on a 25 km scale in the midlatitude North Atlantic. The analysis method uses satellite SST data and an improved version of the inverse method introduced in Chapter 3 (Jeffress and Haine, 2014b). The major improvement is an alternative derivation that allows us to account for a time-continuous forcing with non-zero decorrelation time which is more realistic than the discrete-time white noise forcing used in the model in Jeffress and Haine (2014b). Another improvement is a procedure to estimate errors in the method. The procedure divides the error into two parts: a sample rate error due to the finite sampling time of the observed data, and a convergence error due to the finite timeseries length. The sample rate error is estimated analytically and the convergence error is estimated empirically.

4.2 Mathematical framework

The inversion method works by assuming a continuous-time, discrete-space form of the SST anomaly evolution equation,

$$\frac{d}{dt}\mathbf{c}(t) - \mathbf{B}\mathbf{c} = \mathbf{f}(t). \tag{4.1}$$

Here the $M \times 1$ vector $\mathbf{c}(t)$ is the SST anomaly from the mean climatological value at M spatial locations. The $M \times 1$ vector $\mathbf{f}(t)$ is a stochastic forcing that provides the sources and sinks of SST anomaly variability at the same M locations (Jeffress and Haine, 2014a).

The constant $M \times M$ matrix $\mathbf{B}$ in (4.1) is the transport operator. This matrix is a spatial discretization of the time-averaged advection, diffusion, and decay terms in the partial differential equation (PDE),

$$\frac{\partial}{\partial t}c(\mathbf{x},t) + \nabla_{\mathrm{H}} \cdot [\mathbf{u}(\mathbf{x})c] - \nabla_{\mathrm{H}} \cdot [\boldsymbol{\kappa}(\mathbf{x})\nabla c] - r(\mathbf{x})c = f(\mathbf{x},t). \tag{4.2}$$

Here ∇_{H} is the horizontal gradient and the velocity vector $\mathbf{u} = [u, v]$, diagonal diffusivity tensor $\boldsymbol{\kappa} = [\kappa^x, 0; 0, \kappa^y]$, and decay rate r vary over two-dimensional Cartesian space $\mathbf{x} = [x, y]$. The variables representing physical quantities in (4.2) are averages over the spatial scale $\Delta\mathbf{x} = [\Delta x, \Delta y]$ that is used in the discretization (4.1). The continuous variables $c(\mathbf{x}, t)$ and $f(\mathbf{x}, t)$ are the average SST anomaly and average forcing over $\Delta\mathbf{x}$. The forcing is assumed to have a decorrelation timescale that is short compared to that of SST anomalies (Frankignoul, 1985). The diffusivity $\boldsymbol{\kappa}$ is a parameterization of all molecular and turbulent mixing processes occurring at or below the scale $\Delta\mathbf{x}$; the velocity $\mathbf{u}$ is the average velocity over $\Delta\mathbf{x}$; and the decay rate r is the rate at which SST anomalies averaged over $\Delta\mathbf{x}$ decay to the atmospheric temperature. Eqn.(4.1) is stable if the discretization of (4.2) produces a $\mathbf{B}$ whose eigenvalues have negative real parts.

4.2.1 Inverse method

Now consider that we have observations of $\mathbf{c}(t)$ and wish to estimate $\mathbf{B}$ by applying an inverse method to the observations. The method presented below accomplishes this with an accuracy that depends on the sparsity of $\mathbf{B}$, the intrinsic timescales of $\mathbf{B}$, the forcing decorrelation time τ_f, the SST anomaly decorrelation time τ_c, the timeseries sampling time Δt, and the timeseries length $N\Delta t$. No dynamical constraints on the velocity, diffusivity, or relaxation rate are built in to the inverse method.

The sparsity of $\mathbf{B}$ is determined by the discretization stencil used to estimate the spatial derivatives in (4.2). If the stencil uses K local neighbors with $K \ll M$, then $\mathbf{B}$ is sparse because the i^{th} row $\mathbf{B}_i$ has only K non-zero elements. Although we use a five-point ($K = 5$) discretization stencil in this study, it is instructive to outline the procedure for any $K \ll M$. The sparse structure of $\mathbf{B}$ allows an element of (4.1),

$$\frac{d}{dt}c_i(t) = \mathbf{B}_i\mathbf{c} + f_i(t), \tag{4.3}$$

to be expressed using only a subset of $\mathbf{B}_i$ and $\mathbf{c}$,

$$\frac{d}{dt}\gamma_j(t) = \boldsymbol{\beta}\boldsymbol{\gamma} + f_i(t). \tag{4.4}$$

Here the $1 \times K$ row vector $\boldsymbol{\beta}$ contains the *stencil-elements* of $\mathbf{B}_i$ (in other words the K non-zero elements of $\mathbf{B}_i$). Similarly the $K \times 1$ column vector $\boldsymbol{\gamma}$ contains the corresponding stencil-elements of $\mathbf{c}$. This notation requires $\boldsymbol{\gamma}$ to contain c_i as its j^{th} element $c_i = \gamma_j$. The dependence of $\boldsymbol{\beta}$ and $\boldsymbol{\gamma}$ on row i is suppressed for notational convenience.

The objective now is to estimate $\boldsymbol{\beta}$ using $\boldsymbol{\gamma}$. We accomplish this using covariances lagged by the forcing decorrelation time τ_f. Multiplying (4.4) by $\boldsymbol{\gamma}^{\mathrm{T}}(t-\tau_f)$ and averaging over time yields

$$\left\langle \frac{d\gamma_j(t)}{dt}\boldsymbol{\gamma}^{\mathrm{T}}(t-\tau_f)\right\rangle = \boldsymbol{\beta}\left\langle \boldsymbol{\gamma}(t)\boldsymbol{\gamma}^{\mathrm{T}}(t-\tau_f)\right\rangle + \left\langle f_i(t)\boldsymbol{\gamma}^{\mathrm{T}}(t-\tau_f)\right\rangle . \tag{4.5}$$

Here $^{\mathrm{T}}$ means transpose and the angle brackets $\langle\cdot\rangle$ denote the average over a time period that is very long compared to all other timescales in the problem. The covariance $\left\langle f_i(t)\boldsymbol{\gamma}^{\mathrm{T}}(t-\tau_f)\right\rangle$ vanishes because it is lagged by the forcing decorrelation time. See Appendix 4.A for the derivation. The result is an expression for $\boldsymbol{\beta}$ in terms of $\boldsymbol{\gamma}$,

$$\boldsymbol{\beta} = \left\langle \frac{d\gamma_j(t)}{dt}\boldsymbol{\gamma}^{\mathrm{T}}(t-\tau_f)\right\rangle \left\langle \boldsymbol{\gamma}(t)\boldsymbol{\gamma}^{\mathrm{T}}(t-\tau_f)\right\rangle^{-1} . \tag{4.6}$$

Now consider that our observations of $\mathbf{c}(t)$ are a finite length, discretely-sampled timeseries $\mathbf{c}(n\Delta t)$ for $n = 1, 2, 3, ...N$ at sampling time Δt (perhaps with an unbiased random measurement error). Replace the continuous-time derivative $\frac{d\gamma_j}{dt}$ in (4.6) with a finite difference over the sampling time,

$$\boldsymbol{\beta} + \epsilon_{\Delta t} = \left\langle \frac{\gamma_j(t+\Delta t) - \gamma_j(t)}{\Delta t} \boldsymbol{\gamma}^{\mathrm{T}}(t-\tau_f) \right\rangle \left\langle \boldsymbol{\gamma}(t)\boldsymbol{\gamma}^{\mathrm{T}}(t-\tau_f) \right\rangle^{-1}. \qquad (4.7)$$

Here the sample rate error $\epsilon_{\Delta t}$ is the error from replacing the continuous-time derivative by the finite time difference over the sampling time. Assuming $|\mathbf{B}\Delta t| < 1$ an estimate of this error is

$$\hat{\epsilon}_{\Delta t} = \frac{\hat{\mathbf{B}}^2 \Delta t}{2!} + \frac{\hat{\mathbf{B}}^3 \Delta t^2}{3!} \qquad (4.8)$$

given the estimate $\hat{\mathbf{B}}$ described below. See Appendix 4.B for the derivation.

The fact that the timeseries is finite requires us to replace the long-time average in (4.7) with the average over N samples, denoted by the overbar $[\bar{\cdot}]$,

$$\hat{\boldsymbol{\beta}} = \boldsymbol{\beta} + \epsilon_{\Delta t} + \epsilon_N = \left[\overline{\frac{\gamma_j(t+\Delta t) - \gamma_j(t)}{\Delta t} \boldsymbol{\gamma}^{\mathrm{T}}(t-\tau_f)} \right] \left[\overline{\boldsymbol{\gamma}(t)\boldsymbol{\gamma}^{\mathrm{T}}(t-\tau_f)} \right]^{-1}. \qquad (4.9)$$

Here the convergence error ϵ_N is the error due to estimating and inverting the covariances computed for N samples. This error decreases with the number of independent samples in $\mathbf{c}(n\Delta t)$. The number of independent samples is $N\Delta t/\tau_c$ where τ_c is the decorrelation time of $\mathbf{c}(t)$. However, ϵ_N is not a simple function of the length of the times series because a noisy covariance will often lead to an ill-conditioned matrix inverse. In other words, the covariance estimated from a shorter time-series is more likely to have an ill-conditioned matrix inverse than that estimated from a longer time-series. The ill-conditioned concern is also greater for larger discretization stencils. The reason is that the estimated covariance from a larger (less local) stencil will contain more noise than that from a smaller (more local) stencil for a given length $N\Delta t$. Therefore ϵ_N resists an analytic expression. We quantify ϵ_N empirically by showing the change in $\hat{\boldsymbol{\beta}}$ as one decreases the number of samples N used to estimate the covariances.

Iterating (4.9) for all M elements of $\mathbf{c}$ completes the estimated transport operator $\hat{\mathbf{B}}$. Note that this process can be carried out with minimal computing resources as it requires only M matrix inversions of size $K \times K$. This efficiency is important because it avoids the burdensome inversion of the global $M \times M$ covariance that is required by other implementations of the fluctuation-dissipation approach (Jeffress and Haine, 2014b). It also allows easy application to a global scale or higher resolution dataset because the required computation scales linearly with the number of grid points and can be done in parallel.

4.2.2 Response function

A major advantage of assuming a continuous-time form of the SST transport equation (4.1), is the ability to estimate the analytic response function (Green's function) from an estimate of $\mathbf{B}$. The $M \times M$ response function $\mathbf{G}(t)$ is the solution to (4.1) for an impulsive SST anomaly at each location,

$$\frac{d}{dt}\mathbf{G}(t) - \mathbf{B}\mathbf{G} = \mathbf{I}\delta(t). \tag{4.10}$$

The solution of (4.10) is $\mathbf{G}(\tau) = \mathrm{e}^{\mathbf{B}\tau}$ so the estimate is

$$\hat{\mathbf{G}}(\tau) = \mathrm{e}^{\hat{\mathbf{B}}\tau}. \tag{4.11}$$

Here $\mathrm{e}^{\hat{\mathbf{B}}\tau}$ is a matrix exponential and $\mathbf{I}\delta(t)$ is an $M \times M$ identity matrix multiplying a Dirac delta function. Each column of $\mathbf{I}\delta(t)$ is a forcing field that is zero everywhere except for the one location where heat is impulsively injected. Each forcing field gives rise to an SST response field that evolves as a function of elapsed time $\tau = t - t_0$. The SST response fields (for each impulsive forcing) are the columns of $\mathbf{G}(\tau)$. For a particular i and j the element $G_{ij}(\tau)$ provides the distribution of transit times for an impulsive SST source at j to arrive at i. For particular j and τ, $G_{ij}(\tau)$ provides the spatial spread at elapsed time τ that results from an impulsive SST source at j. For this reason $\mathbf{G}(\tau)$ provides a comprehensive quantification of the point-to-point transport of SST throughout the domain.

4.2.3 Velocity, diffusivity and decay rate

The estimate $\hat{\mathbf{B}}$ also provides estimates of the velocity, diffusivity and decay rate fields. The details of this procedure depend on the size and shape of the discretization stencil. In this study we use a five-point stencil because smaller stencils result in less covariance noise (4.9) and the five-point stencil is the smallest stencil that can express the x and y components of the velocity and diffusivity. The elements of $\mathbf{B}$ that result from the five-point stencil discretization of (4.2) are

$$\begin{aligned}
B_{i,\text{right}} &= \frac{\kappa_i^x}{\Delta x_i^2} - \frac{1}{2\Delta x_i}\left(u_i - \frac{\partial \kappa_i^x}{\partial x}\right) \\
B_{i,\text{above}} &= \frac{\kappa_i^y}{\Delta y_i^2} - \frac{1}{2\Delta y_i}\left(v_i - \frac{\partial \kappa_i^y}{\partial y}\right) \\
B_{i,\text{center}} &= -\frac{2\kappa_i^x}{\Delta x_i^2} - \frac{2\kappa_i^y}{\Delta y_i^2} - r_i - \frac{\partial u_i}{\partial x} - \frac{\partial v_i}{\partial y} \\
B_{i,\text{below}} &= \frac{\kappa_i^y}{\Delta y_i^2} + \frac{1}{2\Delta y_i}\left(v_i - \frac{\partial \kappa_i^y}{\partial y}\right) \\
B_{i,\text{left}} &= \frac{\kappa_i^x}{\Delta x_i^2} + \frac{1}{2\Delta x_i}\left(u_i - \frac{\partial \kappa_i^x}{\partial x}\right).
\end{aligned} \tag{4.12}$$

Here the stencil is centered on location i. Right (left) and above (below) are the grid neighbors of i in the positive (negative) direction of x and y, respectively. The parameters u, v, κ^x, κ^y, and r are $M \times 1$ vectors containing the values of the velocity, diffusivity, and decay rate at all M locations. Equation (4.12) is solved for estimates of the parameters given the estimate $\hat{\mathbf{B}}$:

$$\begin{aligned}
\hat{u}_i^* &= u_i^* + \epsilon_{\Delta t}^{u_i^*} + \epsilon_N^{u_i^*} = \Delta x_i \left(\hat{B}_{i,\text{left}} - \hat{B}_{i,\text{right}}\right) \\
\hat{v}_i^* &= v_i^* + \epsilon_{\Delta t}^{v_i^*} + \epsilon_N^{v_i^*} = \Delta y_i \left(\hat{B}_{i,\text{below}} - \hat{B}_{i,\text{above}}\right) \\
\hat{\kappa}_i^x &= \kappa_i^x + \epsilon_{\Delta t}^{\kappa_i^x} + \epsilon_N^{\kappa_i^x} = \frac{\Delta x_i^2}{2}\left(\hat{B}_{i,\text{left}} + \hat{B}_{i,\text{right}}\right) \\
\hat{\kappa}_i^y &= \kappa_i^y + \epsilon_{\Delta t}^{\kappa_i^y} + \epsilon_N^{\kappa_i^y} = \frac{\Delta y_i^2}{2}\left(\hat{B}_{i,\text{below}} + \hat{B}_{i,\text{above}}\right) \\
\hat{r}_i^* &= r_i^* + \epsilon_{\Delta t}^{r_i^*} + \epsilon_N^{r_i^*} = -\hat{B}_{i,\text{center}} - \frac{2\hat{\kappa}_i^x}{\Delta x_i^2} - \frac{2\hat{\kappa}_i^y}{\Delta y_i^2}.
\end{aligned} \tag{4.13}$$

The effective velocity $u_i^* = u_i - \frac{\partial \kappa_i^x}{\partial x}, v_i^* = v_i - \frac{\partial \kappa_i^y}{\partial y}$, and effective decay rate $r_i^* = r_i + \frac{\partial u_i}{\partial x} + \frac{\partial v_i}{\partial y}$ are estimated instead of $\hat{u}_i, \hat{v}_i, \hat{r}_i$ because approximations of $\frac{\partial \kappa_i^x}{\partial x}, \frac{\partial \kappa_i^y}{\partial y}, \frac{\partial u_i}{\partial x}$ and $\frac{\partial v_i}{\partial y}$ add additional error. For notational convenience, we henceforth we remove the asterisk and refer to the effective velocity and effective decay rate as simply the velocity and decay rate. Iterating (4.13) for all M rows of $\hat{\mathbf{B}}$ yields a complete estimate of the velocity field, diffusivity field, and decay rate field. We do not apply the method at boundary locations or impose any boundary conditions. The result is an open boundary that allows SST anomalies to flow freely out of the domain at the edges.

The expected sample rate error $\hat{\epsilon}_{\Delta t}$ (4.8) is decomposed into errors on the individual fields in the same manner as (4.13)

$$\begin{aligned}
(\hat{\epsilon}_{\Delta t}^{u})_i &= \Delta x_i \left[(\hat{\epsilon}_{\Delta t})_{i,\text{left}} - (\hat{\epsilon}_{\Delta t})_{i,\text{right}} \right] \\
(\hat{\epsilon}_{\Delta t}^{v})_i &= \Delta y_i \left[(\hat{\epsilon}_{\Delta t})_{i,\text{below}} - (\hat{\epsilon}_{\Delta t})_{i,\text{above}} \right] \\
\left(\hat{\epsilon}_{\Delta t}^{\kappa^x}\right)_i &= \frac{\Delta x_i^2}{2} \left[(\hat{\epsilon}_{\Delta t})_{i,\text{left}} + (\hat{\epsilon}_{\Delta t})_{i,\text{right}} \right] \\
\left(\hat{\epsilon}_{\Delta t}^{\kappa^y}\right)_i &= \frac{\Delta y_i^2}{2} \left[(\hat{\epsilon}_{\Delta t})_{i,\text{below}} + (\hat{\epsilon}_{\Delta t})_{i,\text{above}} \right] \\
(\hat{\epsilon}_{\Delta t}^{r})_i &= -(\hat{\epsilon}_{\Delta t})_{i,\text{center}} - \frac{2\left(\hat{\epsilon}_{\Delta t}^{\kappa^x}\right)_i}{\Delta x_i^2} - \frac{2\left(\hat{\epsilon}_{\Delta t}^{\kappa^y}\right)_i}{\Delta y_i^2}.
\end{aligned} \tag{4.14}$$

The expected convergence error for the individual fields $\epsilon_N^{u,\kappa,r}$ is estimated empirically by quantifying the change in the estimates as the length of the timeseries is increased.

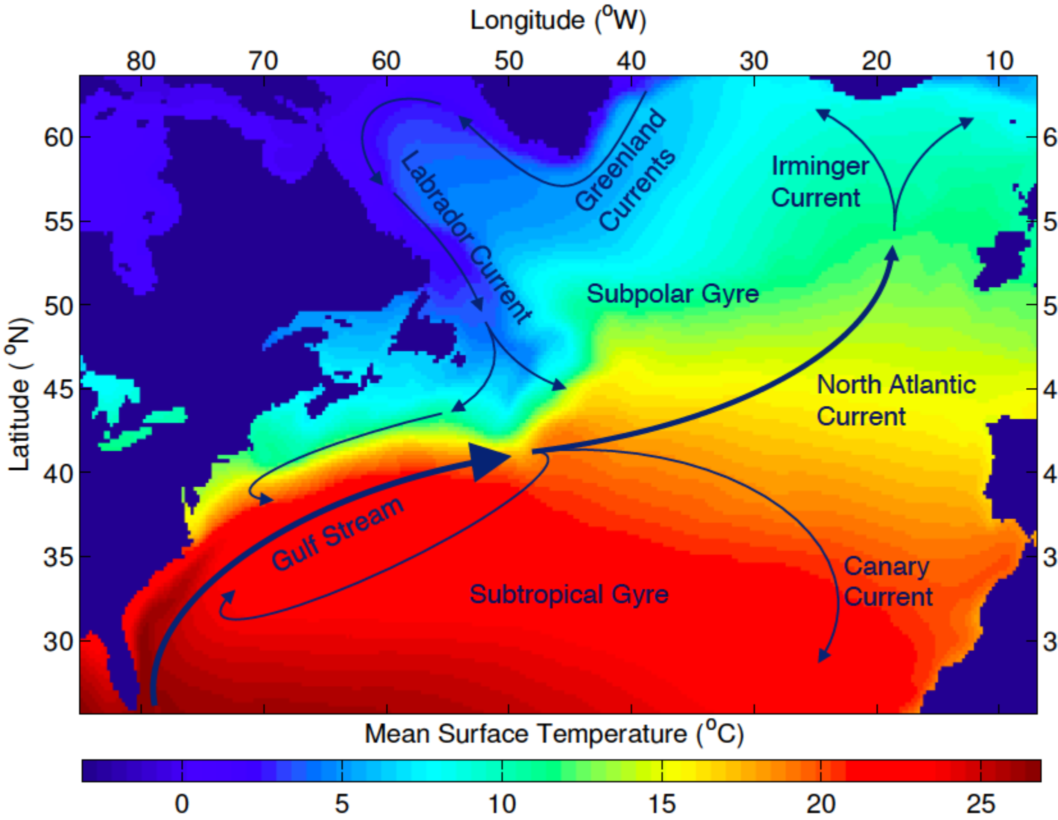

Figure 4.1: Primary surface currents and mean surface temperature of the midlatitude North Atlantic. The circulation is generally cyclonic (counter-clockwise) in the Subpolar Gyre of the northern midlatitudes, and anticyclonic (clockwise) in the Subtropical Gyre of the southern midlatitudes. The color-scale is the time average surface temperature between 1982 and 2013 of the NOAA Optimum Interpolation 1/4 Degree Daily SST Analysis (Reynolds et al., 2007).

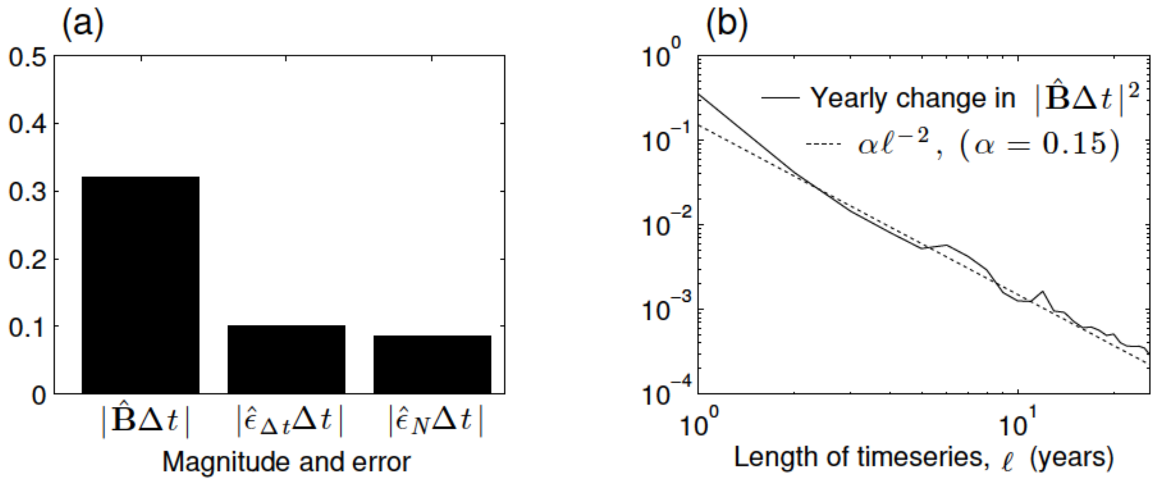

Figure 4.2: Average magnitude and expected error in the transport operator estimate. The expected sample rate error and expected convergence error (a) are $\hat{\epsilon}_{\Delta t} = \pm 34\%$ and $\hat{\epsilon}_N = \pm 21\%$ of the magnitude of $\hat{\mathbf{B}}$, respectively. The yearly change in $|\hat{\mathbf{B}}\Delta t|^2$ (b) is approximately $0.15\ell^{-2}$ where ℓ is the length of the timeseries used. See the text for details of the error calculation.

4.3 Application to North Atlantic SST

This section applies the inversion method to the North Atlantic region of the NOAA Optimum Interpolation 1/4° Daily SST Analysis (Reynolds et al., 2007). This dataset was chosen after experimenting with several alternatives including the GHRSST CMC 0.2° Daily, HadISST 1° Monthly, NCDC 2° Monthly, and Kaplan Extended 5° Monthly reanalysis products. The NOAA Optimum Interpolation dataset is chosen because of its high spatial resolution, uniform sampling, minimal filtering, complete spatial coverage, and long (over 30 years) historical timeseries. The time and space range in this analysis is 1-Jan-1982 to 31-Dec-2013 and 25°N to 65°N and 5°W to 85°W. Figure 4.1 shows the mean surface temperature and the large scale circulation features of the region.

4.3.1 Estimated transport operator

The SST transport operator $\mathbf{B}$ is estimated by applying (4.9) to the SST anomaly timeseries. The anomaly series is obtained by removing the mean, linear trend, and daily climatology at each grid location. The daily climatology is the average temperature for each calendar day in the time range.

Equation (4.9) requires an estimated forcing decorrelation time for which we use $\tau_f = 3$ days (Frankignoul, 1985). The reason is that the forcing of SST anomalies includes anomalies in the net surface-atmospheric heat flux, anomalous advective currents, anomalies in the mixed-layer depth, anomalies in the temperature jump in the entrainment zone, anomalies in the entrainment velocity, anomalies in surface wind stress, and anomalies in the turbulent eddy diffusivity (Frankignoul, 1985). The confluence of these anomalies creates a turbulent forcing that is estimated to have a short decorrelation time of only a few days (Frankignoul et al., 1998; Piterbarg and Ostrovskii, 1997). The appropriateness of $\tau_f = 3$ days is checked at the end of the procedure by using the estimate $\hat{\mathbf{B}}$ together with the observations $\mathbf{c}$ to produce a best fit forcing. The assumption is verified as the decorrelation time of the best fit forcing turns out to be 1 to 2 days.

For each grid cell, equation (4.9) uses the anomaly timeseries of the cell and its neighbors, $\gamma(t)$, to estimate the elements of $\mathbf{B}$ that act on the SST anomaly at that location. The $|\mathbf{B}\Delta t| < 1$ assumption in (4.9) limits the maximum velocity, diffusivity, and decay rates because the largest magnitudes in $\mathbf{B}$ occur with the fastest velocity, diffusivity, and decay in (4.12),

$$\max\left(|\mathbf{B}\Delta t|\right) = \max\left(\frac{\kappa_{\max}}{\Delta x^2} + \frac{u_{\max}}{2\Delta x}, \frac{4\kappa_{\max}}{\Delta x^2} + r_{\max}\right)\Delta t < 1. \tag{4.15}$$

The corresponding upper limits on the velocity, diffusivity, and decay rates for $\Delta x =$ 25 km, $\Delta t = 1$ day are approximately

$$\begin{aligned} u_{\max} &\approx 1\,\mathrm{m/s} \\ \kappa_{\max} &\approx 3,000\,\mathrm{m}^2/\mathrm{s} \\ r_{\max} = &\approx 0.3\,\mathrm{days}^{-1}. \end{aligned} \tag{4.16}$$

Estimates from previous studies suggest that these limits are larger than the typical current speeds, eddy-diffusivities, and SST decay rates in this region (see section 4.3.3). Also the average magnitude of the estimated transport operator is $|\hat{\mathbf{B}}\Delta t| = 0.32$ (Fig. 4.2a). Thus we expect our estimate to be accurate within the sources of error $\hat{\epsilon}_{\Delta t}$ and $\hat{\epsilon}_N$.

The error estimates $\hat{\epsilon}_{\Delta t}$ and $\hat{\epsilon}_N$ are shown in Fig. 4.2. The average magnitude of the expected sample rate error $|\hat{\epsilon}_{\Delta t}| \approx \left|\frac{\hat{\mathbf{B}}^2\Delta t}{2!} + \frac{\hat{\mathbf{B}}^3\Delta t^2}{3!}\right|$ is 34% of $\hat{\mathbf{B}}$. The off-stencil elements of $\hat{\epsilon}_{\Delta t}$ (an additional source of error) are neglected as their magnitude is less then 5% of the stencil elements of $\hat{\mathbf{B}} + \hat{\epsilon}_{\Delta t}$. See Appendix 4.B for the derivation of $\hat{\epsilon}_{\Delta t}$. The yearly change in $|\hat{\mathbf{B}}\Delta t|^2$ (Fig. 4.2b) is approximately $0.15\ell^{-2}$ where ℓ is the length of the timeseries used in the estimate. Integrating $0.15\ell^{-2}$ over the years to come ($-0.15\ell^{-1}$ from 32 to ∞ years) suggests that the average magnitude in the convergence error $\hat{\epsilon}_N$ is 21% of $\hat{\mathbf{B}}$.

4.3.2 Estimated response function

The estimated response function $\hat{\mathbf{G}}(\tau)$ is calculated via (4.11) using $\hat{\mathbf{B}}$ and the default `expm` function in the R2012b version of Matlab. The response function comprehensively quantifies the point-to-point transport of SST anomalies. Figure 4.3 shows portions of $\hat{G}_{iA}(\tau)$ that depict the North Atlantic response from an impulsive SST anomaly just off the southeastern coast of Florida (location A in the top-left panel). The upper six panels are $\hat{G}_{iA}(\tau)$ for all i and at τ = 3 days, 1 month, 3 months, 1 year, 3 years, and 7 years. The arrival time plot below the colorbar shows the times that $\hat{G}_{iA}(\tau)$ arrives at the locations i = B,C,D,E which are identified in the top left panel.

The upper six panels of Fig. 4.3 reveal the individual effects of advection, diffusion and decay as the response spreads throughout the North Atlantic. The effect of advection is most evident in the 6 month response (top right panel). Here the Gulf Stream current is responsible for both the asymmetry of the response pattern as well as the displacement of its center. The angled shape of the response is due to the curvature of the Gulf Stream in this region. The asymmetry is not a result of boundary conditions on the North American coast. We do not impose boundary conditions which means the response flows freely out of the domain. The other evidence of advection is the displacement of the peak response location. If the transport were only diffusive, the center of magnitude of the response would remain centrally located while it spreads

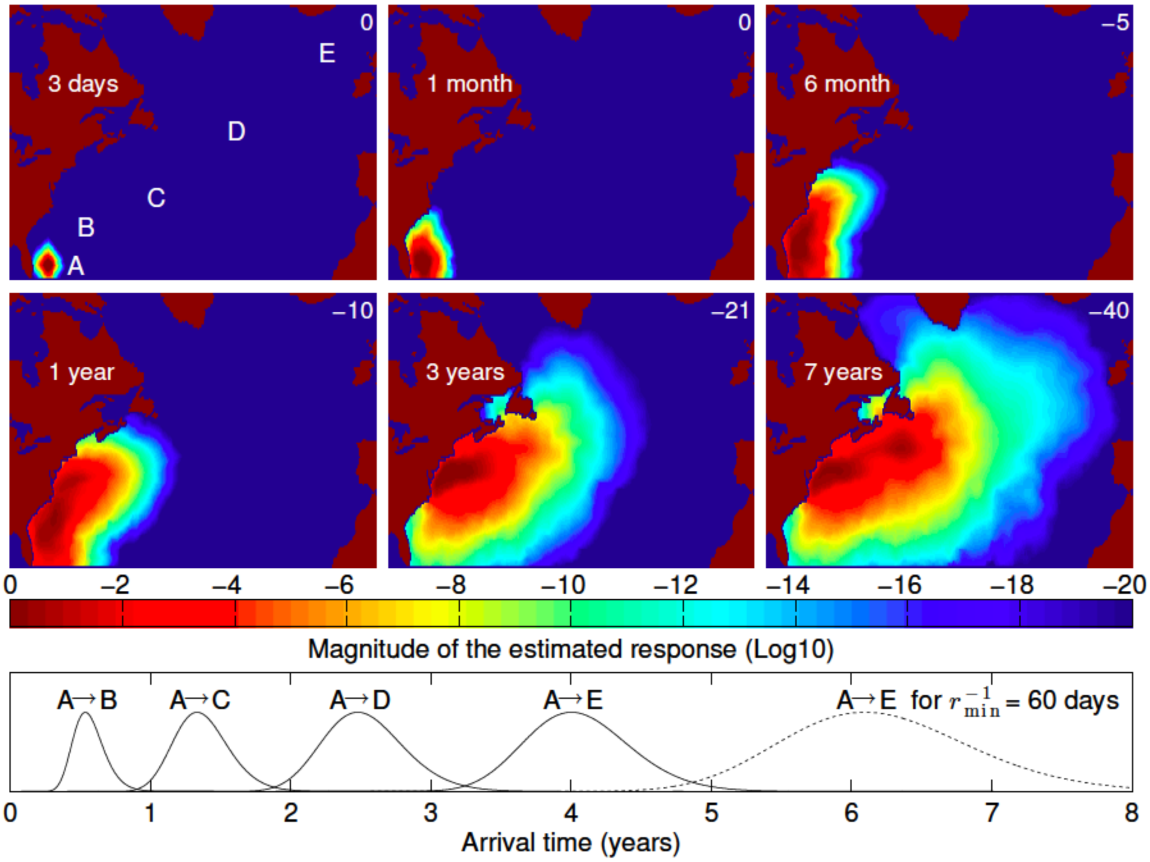

Figure 4.3: Estimated SST response from a 25 km impulse in the Gulf Stream. The impulse occurs at location A (top-left panel) off the south-east coast of Florida. The upper six panels show the estimated response $\hat{G}_{iA}(\tau)$ over all i locations and at $\tau = 3$ days, 1 month, 3 months, 1 year, 3 years, and 7 years. Note that the colorbar is the normalized log (base 10) of $\hat{G}_{iA}(\tau)$. The normalization exponent is in the upper right corner of each panel. The plot below the colorbar shows the distribution of arrival times (solid lines) in $\hat{G}_{iA}(\tau)$ for $\tau = 1$ to 8 years and for locations $i =$ B,C,D,E (identified in the upper left panel). The arrival time distributions are normalized by their modal response magnitude. The dotted arrival time distribution is the normalized $\hat{G}_{EA}(\tau)$ that is produced by restricting decay rates faster than r^{-1} = 60 days in the estimated transport operator.

outward. The spatially dependent decay rates affect the location of the peak response, but this only begins to take effect after the first year when the normalization factor (upper right corner of each panel) drops significantly.

The impact of diffusion is evident in the symmetric spreading of the response throughout the 7 year progression. After only 3 days (top left panel) the bidirectional transport is already apparent. Given the symmetry of the response propagation in the later years and northern midlatitudes, it appears that diffusive spreading is the primary driver of horizontal SST transport outside of the Gulf Stream region. The large range of magnitudes shown by the log10 colorbar reveals the well known unphysical nature of the classical diffusion model, i.e. the infinite speeds of travel of extremely small quantities.

The decay of SST anomalies is the dominant mechanism in the response after the first year as shown by the large decrease in the response magnitude (normalization factor top right corner of each panel). From years 1 to 7 (lower 3 panels in Fig. 4.3), advection and diffusion continue the transport into the North Atlantic, but the maximum response decays by 30 orders of magnitude. This suggests that after 7 years there is essentially nothing remaining of a 25 km SST impulse.

The fast decay rate has a significant impact on the arrival times shown in the plot below the colorbar in Fig. 4.3. Intuitively, the response arrives sooner (later) at the locations that are closer (further) to the impulse. The A→B arrival time distribution suggests that the most common travel time from A to B is less than a year. The A→E response suggests a 4 year modal travel time for the tiny fraction (10^{-40}) of a 25 km SST impulse that survives the coast-to-coast journey from the start of the Gulf Stream to the end of the North Atlantic Current.

The distribution of arrival times cannot be easily decomposed into the effects of advection, diffusion and decay. It is not the case (as one might expect) that the delay in the peak arrival time is due primarily to advection, that the width of the distribution is due only to diffusion, or that the magnitude of the peak response is determined by the decay rate. Instead each of these quantities results from a complex interaction among the mechanisms.

We suspect that a slower decay of larger SST anomalies is the primary reason that our ∼4 year A→E transit time is twice as fast as the ∼8 year transit time found by Hansen and Bezdek (1996) and Sutton and Allen (1997). These studies estimate the travel time using the time lagged correlation of 5-year averaged, winter-time only SST anomalies. One reason for the slower travel times is that low pass filtering the timeseries hinders ones ability to detect the faster transport processes in the inverse problem. However, we suspect the more important difference stems from the finding that large scale SST anomalies decay at a slower rate than smaller scale anomalies (Frankignoul, 1985; Kleeman and Power, 1995). This effect is enhanced by the use of winter-time only data because of the re-emergence of winter-time SST anomalies (Junge and Haine, 2001; de Coëtlogon and Frankignoul, 2003; Zhao and Haine, 2005). The winter-time re-emergence effectively lengthens the average SST anomaly persistence time. To illustrate the effect of longer persistence times, we plot (with a dotted line) the A→E arrival time distribution that results from restricting decay rates faster than r^{-1} =60 days in the estimated transport operator. In addition to an increased magnitude of the response (not shown due to the normalization), the slower decay rate results in a delayed peak arrival time and a widening of the distribution. Section 4.3.3 quantifies the decay rate in detail and further discusses its dependence on the spatial scale of the anomaly.

4.3.3 Estimated fields of velocity, diffusivity, and decay

The estimated transport operator also provides an estimate of the velocity, diffusivity, and decay rate fields. The elements of $\hat{\mathrm{B}}$ are the coefficients of the five-point stencil discretization of the advection-diffusion-decay PDE (4.2). The 5 coefficients at each location are solved for the 2-component velocity, 2-component diffusivity and scalar decay rate at each location (4.13). The resulting estimates are presented in Fig. 4.4. The panels in the figure show the zonal velocity (top left), meridional velocity (top right), average of the zonal and meridional diffusivity (bottom left), and timescale of the decay rate (bottom right). The error estimates are shown in Fig. 4.5. The total expected errors are ∼1.5 cm/s for the velocity fields, ∼550 m^2/s for the diffusivity field, and ∼19 days for the timescale of the decay rate field.

Velocity

The estimated SST velocity field in Fig. 4.4 reflects the large scale circulation of the North Atlantic. As shown in Fig. 4.1, the surface circulation is cyclonic (counter-

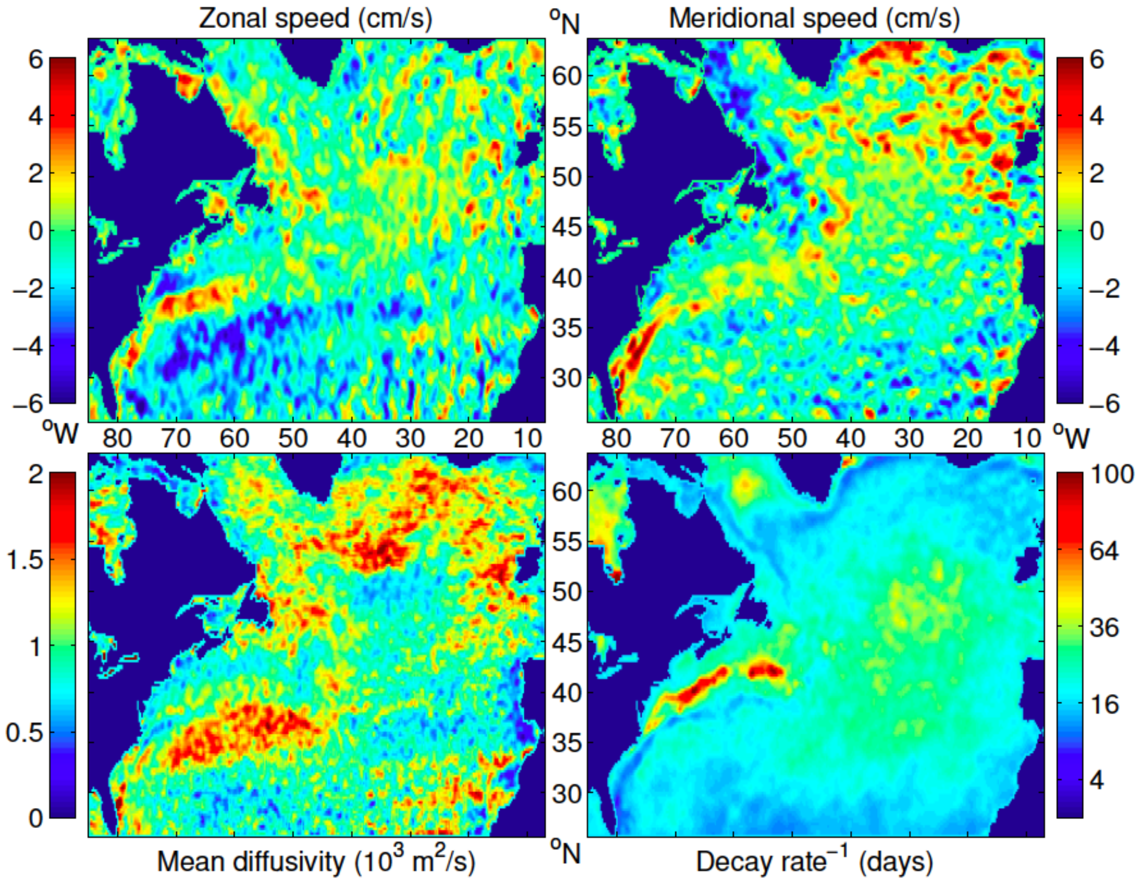

Figure 4.4: Estimated velocities, diffusivities, and decay rates of SST anomalies in the North Atlantic. The zonal speed ($\hat{u}$, upper left, positive east) and meridional speed ($\hat{v}$, upper right, positive north) reflect the general circulation patterns of the Subtropical and Subpolar Gyres (Fig. 4.1). The effective SST speed includes diffusivite gradients which are less than 1 cm/s on average in both the zonal and meridional direction. The average of the zonal and meridional diffusivity (lower left) ranges from 50 m^2/s to 2,000 m^2/s. The average timescale at which SST anomalies decay to the atmospheric temperature (lower right) is 15-40 days except in a small region in the west-central midlatitudes where it exceeds 100 days. Each field has been smoothed with a 3×3 box car filter to reduce noise.

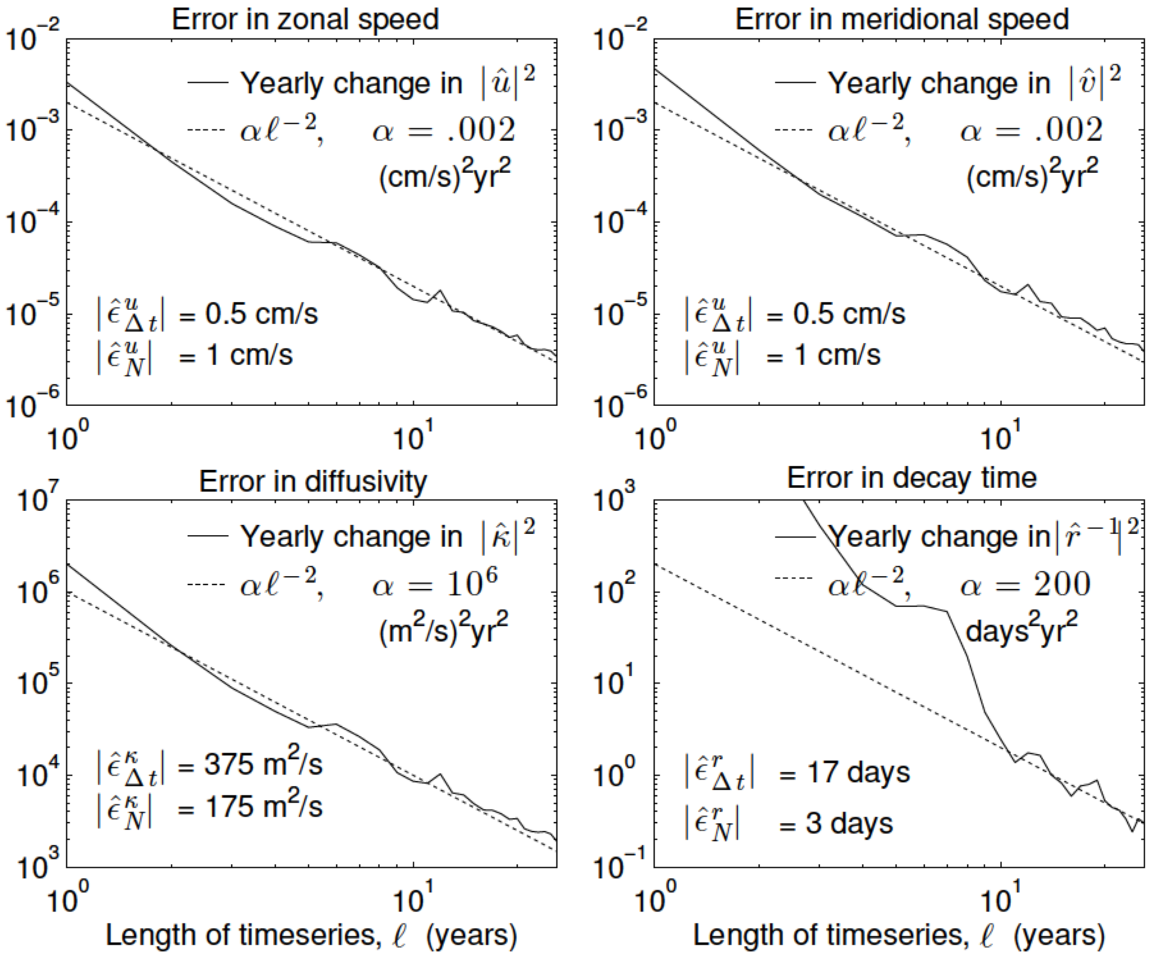

Figure 4.5: Error estimates for Fig. 4.4. The convergence error for each field is quantified by fitting a simple model (dotted lines) to the average yearly change in the squared estimates of each field (solid lines) as the length of the timeseries, ℓ, increases. An estimate of the total convergence errors $|\hat{\epsilon}_N^{u,v,\kappa,r}|$ is obtained by extrapolating each best fit equation ($-\alpha\ell^{-1}$ from 32 to ∞ years). The sample rate error for each field $|\hat{\epsilon}_{\Delta t}^{u,v,\kappa,r}|$ is the average absolute value of $\hat{\epsilon}_{\Delta t}$ (shown in Fig. 4.2) decomposed into the individual transport mechanisms (4.14).

clockwise) in the Subpolar Gyre of the northern midlatitudes and the anticyclonic (clockwise) in the Subtropical Gyre of the southern midlatitudes. The east-west and north-south components of this circulation are evident in the zonal and meridional components of the SST velocity estimates in Fig. 4.4.

The estimated zonal SST speed (top-left panel of Fig. 4.4) is primarily eastward in the central (40°N to 50°N) midlatitudes and westward in the northern (55°N to 65°N) and southern (25°N to 35°N) midlatitudes. The fastest eastward speeds are the components of the Gulf Stream and Labrador Current that combine to form the joint eastward flow of the North Atlantic Current. The westward speeds reflect the recirculating branches of the two gyres in the northern and southern midlatitudes. The strongest westward velocity is just south of the strong eastward component of the Gulf Stream. The velocity of this westward movement is consistent with Halliwell Jr et al. (1991) who found SST anomalies in this region moving westward at $\sim$4 cm/s over the seven year period from 1981-1988. The study could not explain the velocity by the advection of mean currents or by the coincidence of locally correlated atmospheric forcing. Instead the study suggests that westward SST propagation results from a first mode baroclinic rossby wave. Ostrovskii and Font (2003) also suggest a westward propagation in the Subtropical Gyre that is reinforced by planetary waves.

The meridional velocity of SST propagation (top-right panel of Fig. 4.4) is also consistent with the broad scale circulation of the two gyres. The four-square checkerboard pattern is northward in the northeast and southwest midlatitudes, and southward in the northwest and southeast midlatitudes. The strongest southward velocities are seen in the Labrador Current on the western branch of the Subpolar Gyre, and in the Canary Current on the eastern branch of the Subtropical Gyre. The strongest northward velocity is generated by the primary jet of the Gulf Stream off the southeast coast of the United States. The large region of strong northward flow in the northeast midlatitudes is consistent with the direction of the North Atlantic and Irminger Currents, although it is surprising that the speeds in this region are comparable with that of the Gulf Stream. In fact the speed of SST anomalies in most regions are slower than that of the underlying current. In section 4.4 we suggest potential mechanisms for this difference.

Diffusivity

The lower left panel of Fig. 4.4 estimates the average of the zonal and meridional diffusivity. Recall that the diffusivity estimated here is that resulting from the combination of molecular and turbulent diffusion on a 25 km scale. The estimates range from $\sim$50 m^2/s in the eastern midlatitudes to over 2,000 m^2/s in the Gulf Stream and northern midlatitudes. These estimates compare favorably with earlier studies. Ledwell et al. (1998) estimate a 30-300km scale eddy diffusivity of 1000 m^2/s from a sulfur hexaflouride tracer experiment in the eastern North Atlantic main thermocline. Stammer (1998) estimates global eddy diffusivities ranging from 250 m^2/s in quiet parts of the ocean up to 2,500 m^2/s in regions with energetic currents. More recently Zhai and Greatbatch (2006) estimate eddy diffusivities of 1000-2000 m^2/s in the swift currents of the Gulf Stream. Kvaleberg et al. (2008) estimate 500-3000 m^2/s in the western Subpolar Gyre. The high diffusivities in the Gulf stream region of Fig. 4.4 are consistent with our expectations of increased the eddy activity in this region although it is interesting that the high diffusivities are only on the southern side of the Gulf Stream's fastest currents. The high diffusivities in the northern midlatitudes result mostly from the meridional component of the estimated diffusivity tensor (not individually shown) and require further investigation as they do not appear to be associated with known regions of high eddy-activity.

Decay

The lower right panel of Fig. 4.4 estimates the average timescale at which SST anomalies decay. The nonlinear colorbar shows a typical decay timescale of 15 to 40 days, except in a small region in the west-central midlatitudes where it exceeds 100 days. These estimates are consistent with previous studies. The inversion method used by Ostrovskii and Font (2003) estimates anomaly persistence times generally between 23 and 55 days for summertime Gulf Stream SST anomalies averaged over $2^\circ \times 3^\circ$ and 10 days. Frankignoul et al. (1998) estimate anomaly decay times ranging from 30 to 60 days in the summer, and 60 to 120 days in the winter, in the eastern midlatitude North Atlantic using SST anomalies averaged over $5^\circ \times 5^\circ$ and 30 days. The SST anomalies in our study are averaged over $1/4^\circ$ and one day. We suspect this smaller averaging scale is the reason for the shorter persistence times estimated by our study. Larger averaging scales filter out smaller SST anomalies, and smaller SST anomalies have been found to have shorter persistence times. For example Kleeman and Power

(1995) found that SST anomaly persistence times decrease from 185 days to 89 days as the size of the SST anomaly decreases from 1,500 km to 200 km. We also see increased persistence times (not shown) if we smooth the data in time before applying the algorithm. The effect that temporal smoothing has on all estimated fields will be explored in detail in future work.

The long persistence of anomalies in the small region near 43°N, 60°W in Fig. 4.4 has been verified heuristically by watching the 31 year anomaly animation. In the animation it is evident that anomalies persist significantly longer in this region than they do elsewhere. Ostrovskii and Font (2003) also estimate a small region of >100 day persistence times in approximately the same location. In addition to the high diffusivity in the northern midlatitudes and the slow anomaly propagation speed everywhere, the long persistence of anomalies in the 43°N, 60°W region stands out as a phenomenon worth further investigation.

4.4 Discussion

The best-fit velocity field for SST anomaly propagation is unambiguously different from the surface current velocity. The SST speeds in Fig. 4.4 are generally 0-5 cm/s with a maximum of 10 cm/s, where-as the speeds of surface currents from drifter data in this region are generally 30 to 60 cm/s with a maximum of 1 m/s (Richardson, 1983; Fratantoni, 2001). The slow propagation of SST anomalies compared to the underlying current is a phenomenon that has been reproduced by many previous studies. The time lagged correlation analysis of Sutton and Allen (1997) estimates an average Gulf Stream advection speed of 1.7 cm/s. The inverse method of Ostrovskii and Font (2003) estimates SST anomalies propagating northeastward in the Gulf Stream at speeds of 12 cm/s. More recently Chepurin and Carton (2012) use time lagged correlation of satellite based SST anomalies and find an average of advection speed of 2.7 cm/s in the Subpolar Gyre.

We are currently investigating a mechanical explanation for the slow propagation. One candidate mechanism is the blurring of the roles of advection and diffusion at the scale of the anomaly. Mesoscale SST anomalies are not advected like Lagrangian particles. Diffusive spreading causes SST anomalies to migrate out of regions of high velocity (like the Gulf Stream) into the slower-moving adjacent water. This effect retards the net SST anomaly propagation speed (Jeffress and Haine, 2014a). A second potential mechanism is the interaction of SST with the seasonal and main thermocline. This vertical interaction may retard SST anomalies because the currents are weaker at depth (Haine and Richards, 1995; Junge and Haine, 2001; Zhao and Haine, 2005). A third possibility arises from the fact that SST gradients are not randomly aligned with the direction of the surface current. In places where the current is strong (like the Gulf Stream), the SST gradient tends to be perpendicular to the surface (geostrophic) current. Namely, the contours of SST and sea surface height tend to be parallel (referred to as equivalent-barotropic flow). This dynamical effect retards SST anomaly propagation because for perfect SST and SSH alignment, there is no SST advection by the geostrophic current.

4.5 Chapter summary

This chapter has provided insights into the transport of SST anomalies in the midlatitude North Atlantic by applying a fluctuation-dissipation based inverse method to a satellite observed SST dataset. The most significant accomplishment is the empirical estimate of the response function (Green's function) that comprehensively quantifies the transport of SST anomalies between any two locations in the North Atlantic. We advocate the use of this approach to construct response functions of this type in other observational datasets and global circulation models. An additional result is the estimate of the velocity field, diffusivity field, and decay rate field that govern the North Atlantic transport of SST anomalies. Both the response function and estimates of the individual fields agree with previous studies, especially when the interesting effects of averaging scale are taken into consideration. Our estimated errors are reasonable and the 1/4° grid size is the highest spatial resolution of any SST anomaly transport study of which we are aware. The aspect of our study that is least explained by previously known mechanisms, and does not appear to be a consequence of the averaging scale, is the slow speed of SST anomaly propagation compared to that of the underlying currents. Potential mechanisms to explain the slow propagation speed have been proposed and are currently being investigated.

4.6 Chapter appendix

4.A Lagged covariance between SST and forcing

The following argument explains the vanishing lagged covariance in (4.5). The solution for element m of $\boldsymbol{\gamma}^{\mathrm{T}}(t-\tau_f)$ is

$$\gamma_m(t-\tau_f) = \left[\mathbf{c}(t-\tau_f)\right]_n = \left[\int_{-\infty}^{\infty} \mathbf{f}^{\mathrm{T}}(t-\tau_f-t')\mathrm{e}^{\mathbf{B}^{\mathrm{T}}t'}H(t')dt'\right]_n, \tag{4.17}$$

where $\gamma_m = c_n$ as explained in (4.4) and $H(t')$ is the Heaviside step function. Insert (4.17) into the lagged covariance between forcing and SST anomaly in (4.5),

$$\left\langle f_i(t)\boldsymbol{\gamma}^{\mathrm{T}}(t-\tau_f)\right\rangle_m = \left\langle f_i(t)\int_{-\infty}^{\infty} \mathbf{f}^{\mathrm{T}}(t-\tau_f-t')\mathrm{e}^{\mathbf{B}^{\mathrm{T}}t'}H(t')dt'\right\rangle_n. \tag{4.18}$$

Move the time-average inside the integral,

$$\left\langle f_i(t)\boldsymbol{\gamma}^{\mathrm{T}}(t-\tau_f)\right\rangle_m = \left[\int_{-\infty}^{\infty} \left\langle f_i(t)\mathbf{f}^{\mathrm{T}}(t-\tau_f-t')\right\rangle \mathrm{e}^{\mathbf{B}^{\mathrm{T}}t'}H(t')dt'\right]_n. \tag{4.19}$$

The forcing autocorrelation $\left\langle f_i(t)\mathbf{f}^{\mathrm{T}}(t-\tau_f-t')\right\rangle$ vanishes because the forcing is decorrelated at time lags greater than τ_f and $H(t')$ ensures a minimum time separation of τ_f between $f_i(t)$ and $\mathbf{f}^{\mathrm{T}}(t-\tau_f-t')$. Steps (4.17)-(4.19) can be repeated for all m in (4.17).

4.B Derivation of expected sample rate error

The error of approximating $\frac{d}{dt}$ by a finite time difference in (4.7) is shown as follows. The solution for $\gamma_j(t+\Delta t)$ is

$$\gamma_j(t+\Delta t) = [\mathbf{c}(t+\Delta t)]_i \quad = \quad \left[\mathrm{e}^{\mathbf{B}\Delta t}\mathbf{c}(t) + \boldsymbol{\zeta}\right]_i , \tag{4.20}$$

where $\gamma_j = c_i$ as explained in (4.4) and

$$\boldsymbol{\zeta} \quad = \quad \int_0^{\Delta t} \mathrm{e}^{\mathbf{B}(\Delta t - t')}\mathbf{f}(t+t')dt'. \tag{4.21}$$

Subtract $\gamma_j(t)$ from (4.20), multiply by $\frac{1}{\Delta t}\boldsymbol{\gamma}^{\mathrm{T}}(t-\tau_f)$ and average over time,

$$\left\langle \frac{\gamma_j(t+\Delta t) - \gamma_j(t)}{\Delta t}\boldsymbol{\gamma}^{\mathrm{T}}(t-\tau_f)\right\rangle = \frac{1}{\Delta t}\left\langle \left[\left(\mathrm{e}^{\mathbf{B}\Delta t} - \mathbf{I}\right)\mathbf{c}(t) + \boldsymbol{\zeta}\right]_i \boldsymbol{\gamma}^{\mathrm{T}}(t-\tau_f)\right\rangle . \tag{4.22}$$

Element m of the term containing $\boldsymbol{\zeta}$ in (4.22) is

$$\left\langle \zeta_i \left[\boldsymbol{\gamma}^{\mathrm{T}}(t-\tau_f)\right]_m \right\rangle = \left\langle \left[\int_0^{\Delta t} \mathrm{e}^{\mathbf{B}(\Delta t - t')}\mathbf{f}(t+t')dt'\right]_i \left[\boldsymbol{\gamma}^{\mathrm{T}}(t-\tau_f)\right]_m \right\rangle . \tag{4.23}$$

Insert $\gamma_m = c_n$ into (4.23) as explained in (4.4) and move the time average inside the integral,

$$\left\langle \zeta_i \left[\boldsymbol{\gamma}^{\mathrm{T}}(t-\tau_f)\right]_m \right\rangle = \left[\int_0^{\Delta t} \mathrm{e}^{\mathbf{B}(\Delta t - t')}\left\langle \mathbf{f}(t+t')\mathbf{c}^{\mathrm{T}}(t-\tau_f)\right\rangle dt'\right]_{i,n} . \tag{4.24}$$

This expression vanishes for all m because $\mathbf{f}(t+t')$ and $\mathbf{c}^{\mathrm{T}}(t-\tau_f)$ are decorrelated at time-lags of τ_f and greater (see Appendix 4.A). Use this result to simplify (4.22),

$$\left\langle \frac{\gamma_j(t+\Delta t)-\gamma_j(t)}{\Delta t}\boldsymbol{\gamma}^{\mathrm{T}}(t-\tau_f)\right\rangle = \frac{1}{\Delta t}\left\langle \left[\left(\mathrm{e}^{\mathbf{B}\Delta t}-\mathbf{I}\right)\mathbf{c}(t)\right]_i \boldsymbol{\gamma}^{\mathrm{T}}(t-\tau_f)\right\rangle . \tag{4.25}$$

The Taylor Series expansion of $\frac{1}{\Delta t}\left(\mathrm{e}^{\mathbf{B}\Delta t}-\mathbf{I}\right)$ is

$$\frac{1}{\Delta t}\left(\mathrm{e}^{\mathbf{B}\Delta t}-\mathbf{I}\right) = \mathbf{B}+\epsilon_{\text{trunc.}}+\ldots \tag{4.26}$$

where

$$\epsilon_{\text{trunc.}} = \frac{\mathbf{B}^2\Delta t}{2!}+\frac{\mathbf{B}^3\Delta t^2}{3!}. \tag{4.27}$$

We require $|\mathbf{B}\Delta t| < 1$ for the Taylor series elements to decrease in magnitude and for $\epsilon_{\text{trunc.}}$ to be a good approximation of the total truncation error. Inserting (4.26) into (4.25) yields

$$\left\langle \frac{\gamma_j(t+\Delta t)-\gamma_j(t)}{\Delta t}\boldsymbol{\gamma}^{\mathrm{T}}(t-\tau_f)\right\rangle \approx \left\langle \left\{\left[\mathbf{B}+\epsilon_{\text{trunc.}}\right]\mathbf{c}(t)\right\}_i \boldsymbol{\gamma}^{\mathrm{T}}(t-\tau_f)\right\rangle . \tag{4.28}$$

Equation (4.28) requires only the non-zero elements on the i^{th} row of $\mathbf{B}+\epsilon_{\text{trunc}}$. The non-zero elements or "stencil-elements" on the i^{th} row of $\mathbf{B}$ are $\boldsymbol{\beta}$ as described in (4.4). There are additional non-zero elements, "off-stencil elements," in ϵ_{trunc} because $\mathbf{B}^2$ and $\mathbf{B}^3$ reduce sparsity. Provided that $|\mathbf{B}\Delta t| < 1$ however, the magnitude of the off-stencil elements of ϵ_{trunc} are small compared to the stencil elements of $\mathbf{B}+\epsilon_{\text{trunc}}$. This smallness assumption can be tested after obtaining an estimate of $\mathbf{B}$. Neglecting the off stencil elements in (4.28) yields

$$\left\langle \frac{\gamma_j(t+\Delta t)-\gamma_j(t)}{\Delta t}\boldsymbol{\gamma}^{\mathrm{T}}(t-\tau_f)\right\rangle \approx \left\langle \left[\boldsymbol{\beta}+\epsilon_{\text{trunc.}}\right]\boldsymbol{\gamma}(t)\boldsymbol{\gamma}^{\mathrm{T}}(t-\tau_f)\right\rangle . \tag{4.29}$$

Inserting (4.29) into (4.7) yields

$$\boldsymbol{\beta}+\epsilon_{\Delta t} \approx \left[\boldsymbol{\beta}+\epsilon_{\text{trunc}}\right]\left\langle \boldsymbol{\gamma}(t)\boldsymbol{\gamma}^{\mathrm{T}}(t-\tau_f)\right\rangle \left\langle \boldsymbol{\gamma}(t)\boldsymbol{\gamma}^{\mathrm{T}}(t-\tau_f)\right\rangle^{-1} . \tag{4.30}$$

Thus

$$\epsilon_{\Delta t} \approx \epsilon_{\text{trunc.}} \approx \frac{\hat{\mathbf{B}}^2\Delta t}{2!}+\frac{\hat{\mathbf{B}}^3\Delta t^2}{3!} \tag{4.31}$$

is the error associated with the finite difference in (4.7). This error is calculated given the estimate $\hat{\mathbf{B}}$ under the assumption $|\mathbf{B}\Delta t|< 1$, which is checked by computing $|\hat{\mathbf{B}}\Delta t|$.

Chapter 5

Future work

There is a sense that the inverse method developed in this thesis has the potential to revolutionize our understanding of ocean-atmosphere interaction. The reason is that the core algorithm (section 4.2) is highly scalable and easily extends to fluid properties other than SST. A proposal for a broad application of the method has been submitted to NASA under solicitation NNH14ZDA001N-PO. The purpose of the proposal is to diagnose, quantify, and reveal the mechanisms controlling the propagation of anomalies in SST, sea surface salinity (SSS), sea surface chlorophyl (CHL), and sea surface height (SSH). Results from a preliminary investigation are discussed below.

Fig. 5.1 shows the results of applying the method to a climatological SST dataset and a GFDL coupled climate model. The first column shows the velocity components, diffusivity components, and relaxation rates from real SST data using the HadISST climatology (Rayner et al., 2003). The current speeds advecting SST are O(1)cms^{-1},

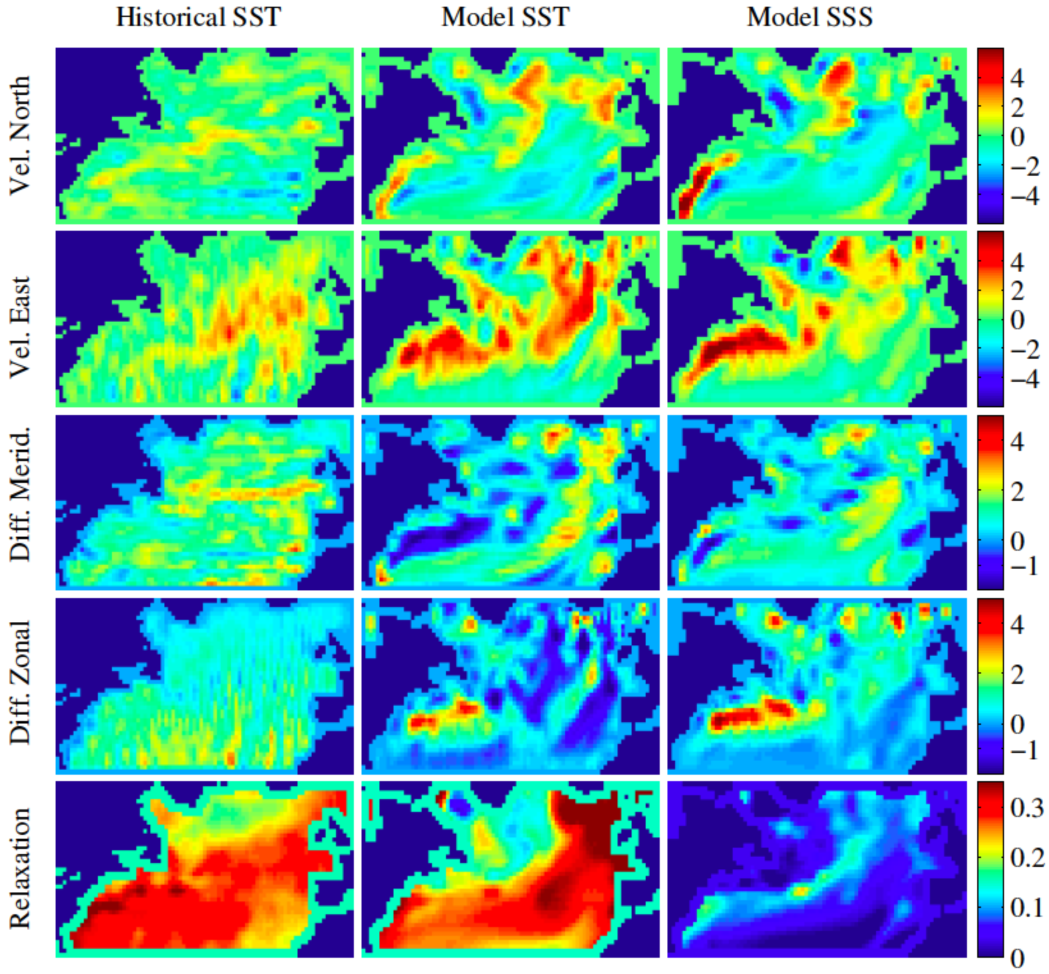

Figure 5.1: Advection, diffusion, and relaxation processes that affect monthly 1° SST and SSS anomalies in the North Atlantic.The historical SST data are from the 1° HadISST product (Rayner et al., 2003); the model SST and SSS output are from a preindustrial control run of the GFDL-CM2.1 coupled climate model (Delworth et al., 2006).

consistent with earlier studies (Sutton and Allen, 1997; Hansen and Bezdek, 1996; Chepurin and Carton, 2012). Similarly, the diffusivity components are O(1000)$\mathrm{m}^2\mathrm{s}^{-1}$, consistent with independent estimates of, for example, Kvaleberg et al. (2008). The relaxation rates are O(0.1) month^{-1}, consistent with Frankignoul et al. (1998). These estimates differ from those obtained from the 1/4° daily satellite data in Chapter 4, however there is no obvious inconsistency because of the different spatial and temporal resolution of the datasets.

The second column of Fig. 5.1 shows the results of applying the method to SST output from a preindustrial control run of the GFDL-CM2.1 coupled climate model (Delworth et al., 2006). The estimated fields of surface velocity advecting SST, diffusivity, and relaxation rate are similar in many ways to the results from data. For example, notice the same patterns of high relaxation rates in the subtropical gyre and northeast Atlantic and low relaxation rates in the subpolar gyre.The magnitudes of the velocity and diffusivity components are also similar. The velocity components show familiar features of the surface flow, like the Gulf Stream, North Atlantic Current, and the gyre recirculations. The details are different, however. The diffusivity components from the SST data and coupled model have similar magnitudes, but different patterns. The diffusivity values from the coupled model, but not the climatology, are negative in some places, indicating upgradient SST diffusion. They potentially reflect positive feedbacks erroneously attributed to diffusion in our framework.

The differences between the real data and model output arise from differences in the advection and diffusion fields in the real ocean and the model. They are not due to

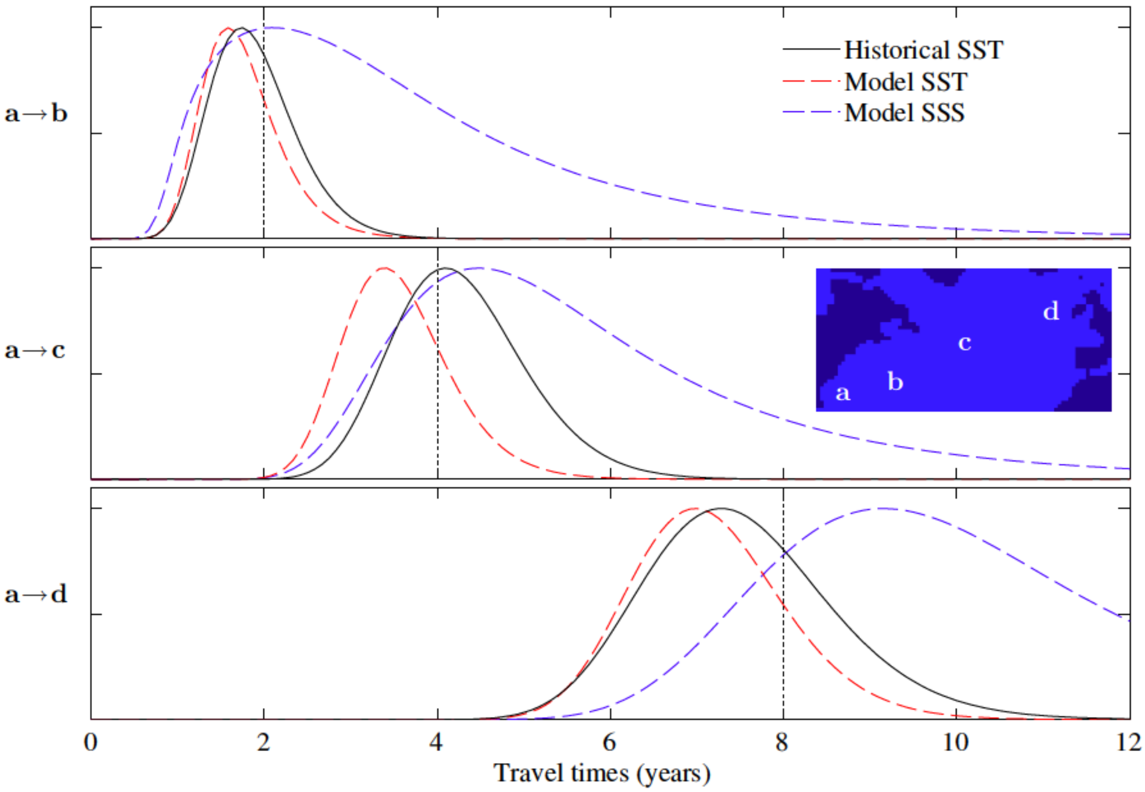

Figure 5.2: Estimated travel time distributions for SST and SSS transport in the Gulf Stream from the response function. As in Fig. 5.1, results from historical SST data and coupled model output are shown.The response functions are all normalized to have identical peak densities. Vertical dashes are the estimates of transport timescale by Sutton and Allen (1997).

limited data length in the HadISST climatology. Indeed, as long as we include the era of satellite SST measurements, the results in Fig. 5.1 are insensitive to the data length.

The new method to infer SST transport fields also provides, uniquely, the SST response function. Figs. 5.2 and 5.3 show elements of this revealing diagnostic for the SST data and model output. Consider Fig. 5.2 first. It shows the distribution over time of responses at points **b**, **c**, and **d** along the North Atlantic Current to an impulsive SST anomaly in the Gulf Stream at point **a**. The response curves from the historical SST data and the model are remarkably similar. They have very similar modal response times, and very similar spreads in response time, which grow wider downstream. Interestingly, this similarity occurs despite the differences in velocity and diffusivity fields seen in Fig. 5.1. Earlier studies on SST anomaly propagation are broadly consistent (e.g., Sutton and Allen (1997): see the vertical dashed lines), but there are two major improvements with the new method: First, these earlier studies quote the time-lag of greatest correlation between SST anomaly timeseries at remote locations. This diagnostic is a biased estimator of the modal response time, however, as explained by Jeffress and Haine (2014a). The response function computed from the new method is unbiased (Jeffress and Haine, 2014b). Second, these earlier studies were unable to estimate the spread of response times, which is clearly substantial from Fig. 5.2.

In Fig. 5.3 a series of response function snapshots is shown for an impulsive forcing in the Gulf Stream at point **a** (for convenience; any point can be chosen). The response function from historical SST data is similar to that from the climate model and reveals the familiar surface circulation dominated by the North Atlantic current and gyres. This diagnostic reveals the power of the new method: analysis of the SST observations produces an empirical estimate of the real ocean's response to impulsive forcing.

Figs. 5.1–5.3 also show preliminary results for SSS from the coupled model. The comparison between SST and SSS results is instructive. First, note in Fig. 5.1 that the velocity and diffusivity fields estimated from SST and SSS model output are

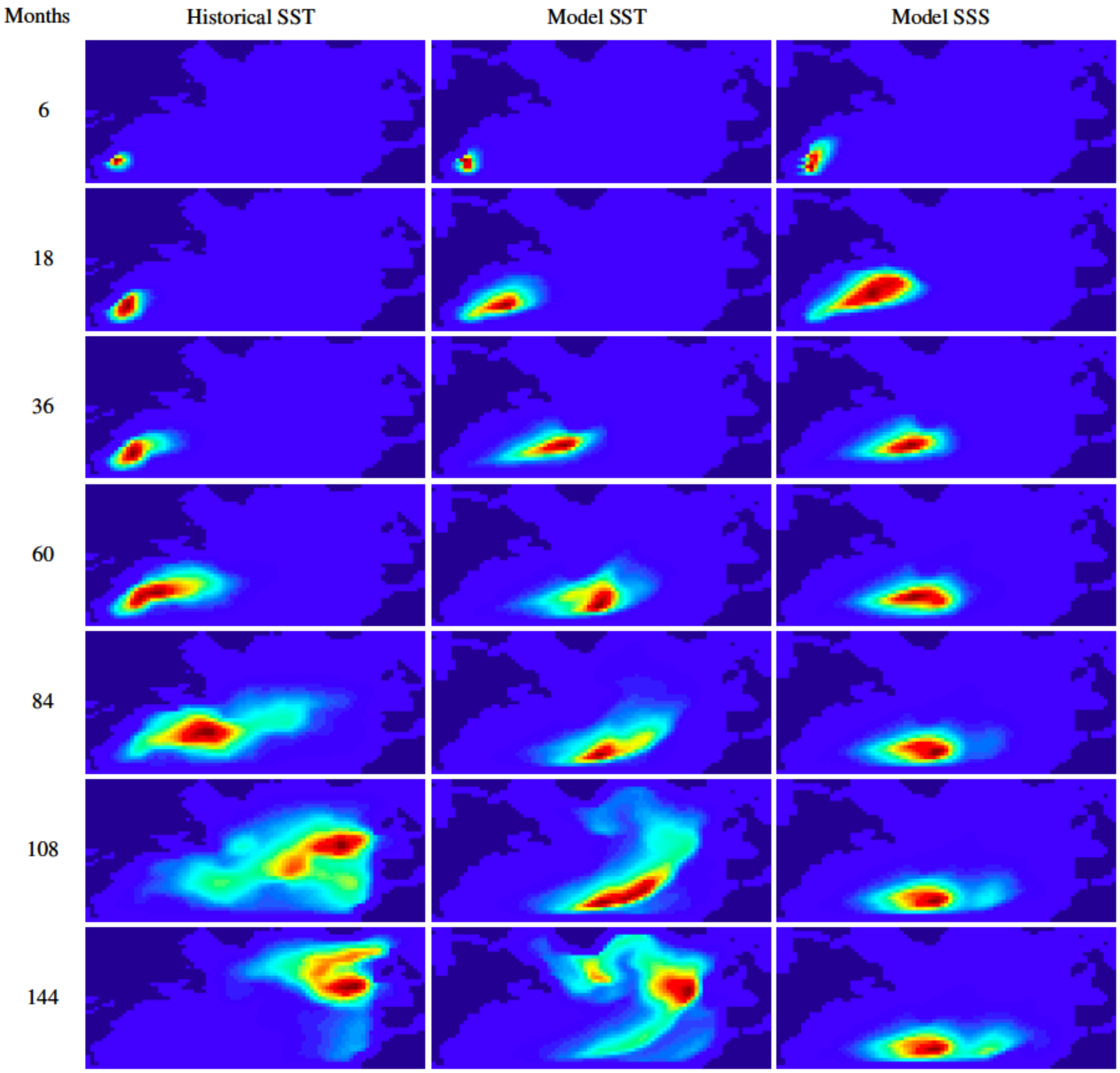

Figure 5.3: Estimated response of North Atlantic SST and SSS over time to impulsive forcing at point **a** (Fig. 5.2) in the Gulf Stream. As in Fig. 5.1, results from historical SST data and coupled model output are shown. The response functions are all normalized to have identical peak densities. For the model, a minimum diffusivity of $500\mathrm{m}^2\mathrm{s}^{-1}$ was used for stability.

very similar. One important exception occurs in the northeast Atlantic zonal current where the speed from the SST analysis is significantly stronger (eastward) than from the SSS analysis. The patch of strong eastward propagation in the northeast Atlantic also occurs in the field estimated from the SST data, indicating that it is a real phenomenon. The origin of this SST propagation is presently unknown. Results from a global calculation using the coarser-resolution ($3^\circ \times 1^\circ$) GFDL-ESM2Mc model (Fig. 5.4) show similar relationships between SST and SSS anomaly propagation in the North Pacific and Southern Ocean. They indicate that this pattern is not simply an artifact either of resolution or of the particular geometry of the North Atlantic.

Second, there is a profound difference in relaxation rates deduced from the SST analysis (which are fast) compared to the SSS analysis (which are slow). The SSS relaxation rates are not zero, however. They are highest in the Gulf Stream and North Atlantic Current, for unknown reasons. The physical mechanisms relaxing SSS anomalies—perhaps exchange with the thermocline—are also unknown. To our knowledge, this SSS relaxation-rate field has never been quantified before.

The weak SSS relaxation rates also influence the response function. In Fig. 5.2 we see that the modal time for response to an SSS impulse is longer than for SST. The spread in response times is also greater with a long tail, unlike SST. In Fig. 5.3 we see SSS anomalies circulate in the Gulf Stream and subtropical gyre, but apparently not in the subpolar gyre. These differences in response function are both explained by the faster SST damping. Faster damping cuts off the long response-function tails for SST in Fig. 5.2. The fast damping is not uniform, however. It is relatively weak in

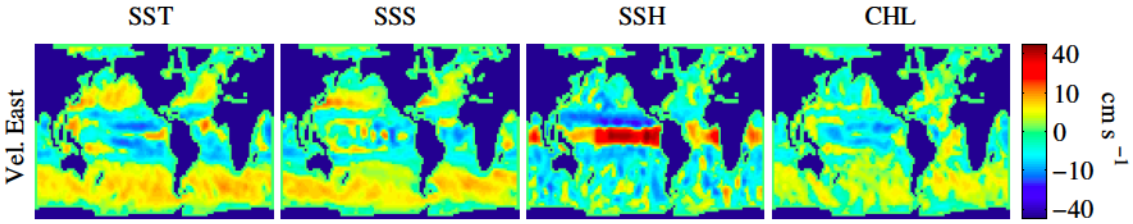

Figure 5.4: Eastward propagation speed of SST, SSS, SSH, and surface chlorophyll anomalies from a preindustrial control run of the coarse-resolution (3° × 1°) GFDL-ESM2Mc model. Note that the scale is nonlinear so as to resolve relatively small off-equatorial velocities.

the subpolar gyre. For this reason, the SST response function in Fig. 5.3 shows higher densities than SSS in that area. The subpolar SST response is relatively long-lived because it relaxes more slowly there. These comparisons between SST and SSS are thought-provoking and illuminate the complex interplay between advection, diffusion, and relaxation in controlling SST and SSS anomalies.

Chapter 6

Conclusion

The following are the major conclusions of the thesis. Midlatitude SST anomalies are well represented as the linear response to a stochastic forcing. The response function that solves the SST continuity equation for an impulsive forcing provides the most comprehensive approach to quantifying SST transport. The impulse response framework clarifies the relationship between correlation and causation because time-lagged correlations are convolutions of the response function and forcing autocorrelation. The time-lag of greatest correlation generally does not estimate the advective time in flows where SST anomalies are advected by currents, diffused by eddies, and relaxed to atmospheric temperatures. A better approach to estimating the response is to fit the linearized dynamics using a local covariance-based inverse method. The linear operator gives the response analytically and is decomposed into a velocity field, diffusivity field, and decay rate field. Results in a two-dimensional model show quick convergence to the true values of the response function, velocity, diffusivity, and decay rates. Application to North Atlantic satellite data produces estimates consistent with previous studies and reveals an unexpected slow propagation of SST anomalies. As far as we know, this thesis provides the first empirically derived estimate of an SST impulse response function. Given its scalability and the potential to apply it to ocean surface properties other than temperature, we believe the inverse method developed in this thesis has the potential to revolutionize our understanding of ocean-atmosphere interaction.

Bibliography

Achatz, U., Löbl, U., Dolaptchiev, S. I., and Gritsun, A. (2013). Fluctuation-dissipation supplemented by nonlinearity: A climate-dependent subgrid-scale parameterization in low-order climate models. *Journal of the Atmospheric Sciences*, 70(6).

Alexander, M. A., Deser, C., and Timlin, M. S. (1999). The reemergence of sst anomalies in the north pacific ocean. *Journal of climate*, 12(8):2419–2433.

Boyce, W. E. and DiPrima, R. C. (1986). *Elementary differential equations and boundary value problems*, volume 4. John Wiley and Sons.

Callen, H. B. and Welton, T. A. (1951). Irreversibility and generalized noise. *Physical Review*, 83(1):34–40.

Chepurin, G. and Carton, J. (2012). Subarctic and Arctic sea surface temperature and its relation to ocean heat content 1982–2010. *Journal of Geophysical Research*, 117(C6):C06019.

Cooper, F. C. and Haynes, P. H. (2011). Climate sensitivity via a nonparametric fluctuation–dissipation theorem. *Journal of the Atmospheric Sciences*, 68(5).

Curry, R. and McCartney, M. (1996). Laborador sea water carries northern climate signal south-subpolar signal appear years later at bermuda. *Oceanus*, 39(2):24–29.

de Coëtlogon, G. and Frankignoul, C. (2003). The persistence of winter sea surface temperature in the north atlantic. *Journal of climate*, 16(9):1364–1377.

Delworth, T. L., Broccoli, A. J., Rosati, A., Stouffer, R. J., Balaji, V., Beesley, J. A., Cooke, W. F., Dixon, K. W., Dunne, J., Dunne, K., et al. (2006). Gfdl's cm2 global coupled climate models. part i: Formulation and simulation characteristics. *Journal of Climate*, 19(5):643–674.

Dickson, R. R., Meincke, J., Malmberg, S.-A., and Lee, A. J. (1988). The great salinity anomaly in the Northern North Atlantic 19681982. *Progress In Oceanography*, 20(2):103 – 151.

Frankignoul, C. (1985). Sea surface temperature anomalies, planetary waves, and air-sea feedback in the middle latitudes. *Reviews of Geophysics*, 23(4):357–390.

Frankignoul, C., Czaja, A., and L'Heveder, B. (1998). Air-sea feedback in the north atlantic and surface boundary conditions for ocean models. *Journal of climate*, 11(9):2310–2324.

Fratantoni, D. M. (2001). North atlantic surface circulation during the 1990's observed with satellite-tracked drifters. *Journal of Geophysical Research: Oceans (1978–2012)*, 106(C10):22067–22093.

Gritsun, A. and Branstator, G. (2007). Climate response using a three-dimensional operator based on the fluctuation–dissipation theorem. *Journal of the atmospheric sciences*, 64(7).

Haine, T. W. and Richards, K. J. (1995). The influence of the seasonal mixed layer on oceanic uptake of cfcs. *Journal of Geophysical Research: Oceans (1978–2012)*, 100(C6):10727–10744.

Haine, T. W. N. and Hall, T. M. (2002). A generalized transport theory: Water-mass composition and age. *Journal of physical oceanography*, 32(6):1932–1946.

Hall, T. and Plumb, R. (1994). Age as a diagnostic of stratospheric transport. *Journal of Geophysical Research-All Series-*, 99:1059–1059.

Halliwell Jr, G. R., Cornillon, P., and Byrne, D. A. (1991). Westward-propagating sst anomaly features in the sargasso sea, 1982-88. *Journal of physical oceanography*, 21(5):635–649.

Hansen, D. V. and Bezdek, H. F. (1996). On the nature of decadal anomalies in north atlantic sea surface temperature. *Journal of Geophysical Research: Oceans (1978–2012)*, 101(C4):8749–8758.

Hasselmann, K. (1976). Stochastic climate models part i. theory. *Tellus*, 28(6):473–485.

Holliday, N., Hughes, S., Bacon, S., Beszczynska-Möller, A., Hansen, B., Lavin, A., Loeng, H., Mork, K., Østerhus, S., Sherwin, T., et al. (2008). Reversal of the 1960s to 1990s freshening trend in the northeast north atlantic and nordic seas. *Geophysical Research Letters*, 35:L03614.

Holzer, M. and Hall, T. M. (2000). Transit-time and tracer-age distributions in geophysical flows. *Journal of the atmospheric sciences*, 57(21):3539–3558.

Jeffress, S. and Haine, T. (2014a). Correlated signals and causal transport in ocean circulation. *Quarterly Journal of the Royal Meteorological Society.*

Jeffress, S. and Haine, T. (2014b). Estimating sea-surface temperature transport fields from stochastically-forced fluctuations. *New Journal of Physics.*

Junge, M. M. and Haine, T. W. (2001). Mechanisms of north atlantic wintertime sea surface temperature anomalies. *Journal of climate*, 14(24):4560–4572.

Kleeman, R. and Power, S. B. (1995). A simple atmospheric model of surface heat flux for use in ocean modeling studies. *Journal of physical oceanography*, 25(1):92–105.

Kvaleberg, E., Haine, T., and Waugh, D. (2008). Middepth spreading in the subpolar north atlantic ocean: Reconciling cfc-11 and float observations. *Journal of Geophysical Research: Oceans (1978–2012)*, 113(C8).

Ledwell, J. R., Watson, A. J., and Law, C. S. (1998). Mixing of a tracer in the pycnocline. *Journal of Geophysical Research: Oceans (1978–2012)*, 103(C10):21499–21529.

Leith, C. (1975). Climate response and fluctuation dissipation. *Journal of the Atmospheric Sciences*, 32(10):2022–2026.

Majda, A., Abramov, R. V., and Grote, M. J. (2005). *Information theory and stochastics for multiscale nonlinear systems*, volume 25. American Mathematical Soc.

Neu, J. L. and Plumb, R. A. (1999). Age of air in a leaky pipe model of stratospheric transport. *Journal of geophysical research*, 104(D16):19243–19.

Newman, M. (2007). Interannual to decadal predictability of tropical and north pacific sea surface temperatures. *Journal of climate*, 20(11).

Nyquist, H. (1928). Thermal agitation of electric charge in conductors. *Physical review*, 32(1):110–113.

Ostrovskii, A. and Font, J. (2003). Advection and dissipation rates in the upper ocean mixed layer heat anomaly budget over the north atlantic in summer. *Journal of Geophysical Research: Oceans (1978–2012)*, 108(C12).

Ostrovskii, A. G. and Piterbarg, L. I. (2000). Inversion of upper ocean temperature time series for entrainment, advection, and diffusivity. *Journal of physical oceanography*, 30(1):201–214.

Penland, C. and Sardeshmukh, P. D. (1995). The optimal growth of tropical sea surface temperature anomalies. *Journal of climate*, 8(8):1999–2024.

Pickart, R. S., Hogg, N. G., and Smethie, W. M. (1989). Determining the strength of the deep western boundary current using the chlorofluoromethane ratio. *J. Phys. Oceanogn, I*, 9:940–951.

Piterbarg, L. and Ostrovskii, A. (1997). *Advection and diffusion in random media: implications for sea surface temperature anomalies.* Springer.

Rayner, N., Parker, D., Horton, E., Folland, C., Alexander, L., Rowell, D., Kent, E., and Kaplan, A. (2003). Global analyses of sea surface temperature, sea ice, and night marine air temperature since the late nineteenth century. *Journal of Geophysical Research: Atmospheres (1984–2012)*, 108(D14).

Rehder, G., Keir, R. S., Suess, E., and Rhein, M. (1999). Methane in the northern Atlantic controlled by microbial oxidation and atmospheric history. *Geophysical Research Letters*, 26(5):587–590.

Reynolds, R. W., Smith, T. M., Liu, C., Chelton, D. B., Casey, K. S., and Schlax, M. G. (2007). Daily high-resolution-blended analyses for sea surface temperature. *Journal of Climate*, 20(22):5473–5496.

Rhein, M. (1994). The deep western boundary current: tracers and velocities. *Deep Sea Research Part I: Oceanographic Research Papers*, 41(2):263–281.

Richardson, P. L. (1983). Eddy kinetic energy in the north atlantic from surface drifters. *Journal of Geophysical Research: Oceans (1978–2012)*, 88(C7):4355–4367.

Ring, M. J. and Plumb, R. A. (2008). The response of a simplified gcm to axisymmetric forcings: Applicability of the fluctuation–dissipation theorem. *Journal of the Atmospheric Sciences*, 65(12).

Snieder, R. (2006). Retrieving the Greens function of the diffusion equation from the response to a random forcing. *Physical Review E*, 74(4):046620.

Stammer, D. (1998). On eddy characteristics, eddy transports, and mean flow properties. *Journal of Physical Oceanography*, 28(4):727–739.

Sutton, R. T. and Allen, M. R. (1997). Decadal predictability of North Atlantic sea surface temperature and climate. *Nature*, 388.

Terenzi, F. and Hall, T. M. (2010). Idealized tracer transport models with time-varying transport: applications to ocean boundary currents. *Environmental fluid mechanics*, 10(1-2):235–255.

Waugh, D. and Hall, T. (2002). Age of stratospheric air: Theory, observations, and models. *Rev. Geophys*, 40(4):1010.

Waugh, D. W. and Hall, T. M. (2005). Propagation of tracer signals in boundary currents. *Journal of physical oceanography*, 35(9):1538–1552.

Yule, G. (1926). Why do we sometimes get nonsense-correlations between time-series?–a study in sampling and the nature of time-series. *Journal of the Royal Statistical Society*, 89(1):1–63.

Zanna, L. (2012). Forecast skill and predictability of observed atlantic sea surface temperatures. *Journal of Climate*, 25(14).

Zhai, X. and Greatbatch, R. J. (2006). Inferring the eddy-induced diffusivity for heat in the surface mixed layer using satellite data. *Geophysical research letters*, 33(24).

Zhao, B. and Haine, T. W. (2005). On processes controlling seasonal north atlantic sea surface temperature anomalies in ocean models. *Ocean Modelling*, 9(3):211–229.

Curriculum Vitae

STEPHEN A JEFFRESS

Email: Jeffress@jhu.edu

Phone: +1(321)368-5312

Address: Johns Hopkins University
Earth & Planetary Sciences
3400 N. Charles St., Olin Hall
Baltimore, MD 21218 USA

Date of Birth: 22 July 1980

EDUCATION

2014, PhD, Johns Hopkins University, Earth and Planetary Sciences

2011, MA, Johns Hopkins University, Earth and Planetary Sciences

2008, MS, University of Central Florida, Industrial Engineering

2005, MS, North Carolina State University, Electrical Engineering

2004, BS, North Carolina State University, Electrical Engineering

PUBLICATIONS

Jeffress, S. and Haine, T. (2014b). Estimating sea-surface temperature transport fields from stochastically-forced fluctuations. *New Journal of Physics.*

Jeffress, S. and Haine, T. (2014a). Correlated signals and causal transport in ocean circulation. *Quarterly Journal of the Royal Meteorological Society.*

CONFERENCE PRESENTATIONS

April 2014, A new method to infer sea-surface temperature anomaly dynamics from stochastic fluctuations, *European Geosciences Union*, Austria, Vienna.

June 2013, Correlated signals and causal transport in ocean circulation, *19th Conference on Atmospheric and Oceanic Fluid Dynamics*, Newport, Rhode Island. (Best Student Paper Award)

May 2013, A climate of curiosity, *NSF Video and Poster Competition for the Integrative Graduate Education and Research Traineeship*, Online. (Judges Choice Award)

March 2013, Transit time distributions in stochastically forced ocean circulation, *Workshop on Modeling and Computing for Weather and Climate Prediction*, Oxford University.

November 2006, Real time anomaly detection for expendable launch vehicles, *International Forum on Integrated System Health Management in Aerospace*, Napa Valley, California.

PROFESSIONAL EXPERIENCE

2005-2009, NASA, Flight Control Engineer, Cape Canaveral, FL

2002-2002, US Senate, Edward M. Kennedy Intern, Washington, DC

2000-2001, Cisco Systems, Engineering Co-op Student, Research Triangle Park, NC

TEACHING EXPERIENCE

2012, Teaching Assistant, *Guided Tour of the Planets*, Johns Hopkins University

2004, Lab Instructor, *Introduction to Computing Environments*, North Carolina State University

FELLOWSHIPS

2010, NSF, Integrative Graduate Education and Research Traineeship

2009, JHU, Earth and Planetary Sciences Obert Fellowship

2008, NASA, Kennedy Graduate Fellowship